HAL
open science

Genesis of a florencite-bearing kaolin deposit on ordovician schists at Saint-Aubin-des-Châteaux, Armorican Massif, France

Anne Gaudin, V. Ansan, Jean-Pierre Lorand, Sylvain Pont

To cite this version:

Anne Gaudin, V. Ansan, Jean-Pierre Lorand, Sylvain Pont. Genesis of a florencite-bearing kaolin deposit on ordovician schists at Saint-Aubin-des-Châteaux, Armorican Massif, France. Ore Geology Reviews, 2020, 120, pp.103445. 10.1016/j.oregeorev.2020.103445 . hal-02961226

HAL Id: hal-02961226

https://hal.science/hal-02961226v1

Submitted on 14 Oct 2020

HAL is a multi-disciplinary open access archive for the deposit and dissemination of scientific research documents, whether they are published or not. The documents may come from teaching and research institutions in France or abroad, or from public or private research centers.

L'archive ouverte pluridisciplinaire **HAL**, est destinée au dépôt et à la diffusion de documents scientifiques de niveau recherche, publiés ou non, émanant des établissements d'enseignement et de recherche français ou étrangers, des laboratoires publics ou privés.

Copyright

Highlights

- The Tertre Rouge kaolin deposit replaces ordovician schists of the Armorican Massif
- Al-phosphates are major concentrators of LREE and Sr
- Kaolinization was mainly produced by Paleogene weathering
- A minor, older hydrothermal event is suggested by high-T clay mineral veinlets

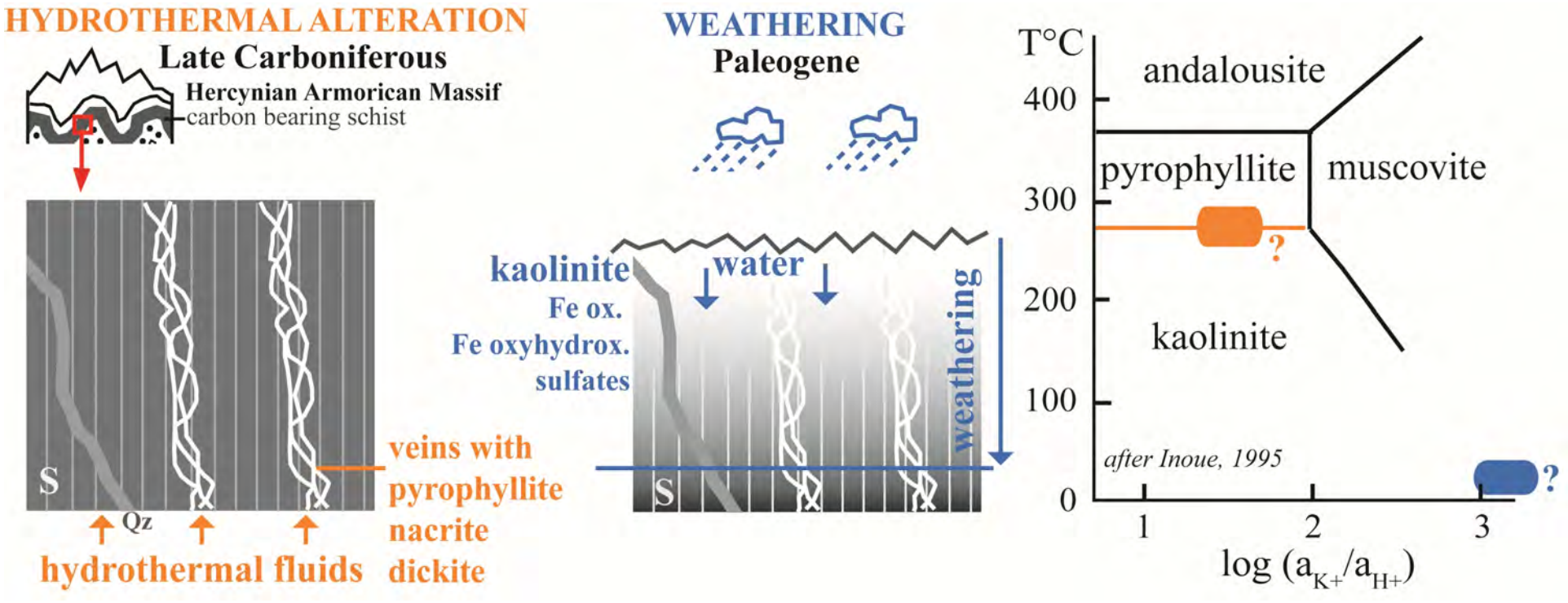
HYDROTHERMAL ALTERATION
Late Carboniferous
Hercynian Armorican Massif
carbon bearing schist
S
Qz
hydrothermal fluids
veins with
pyrophyllite
nacrite
dickite
WEATHERING
Paleogene
kaolinite
Fe ox.
Fe oxyhydrox.
sulfates
water
weathering
S
T°C
400
300
200
100
0
andalousite
pyrophyllite
muscovite
kaolinite
?
?
after Inoue, 1995
1
2
3
log (a_K+/a_H+)

GENESIS OF A FLORENCITE-BEARING KAOLIN DEPOSIT ON ORDOVICIAN SCHISTS AT SAINT-AUBIN-DES-CHATEAUX, ARMORICAN MASSIF, FRANCE

Anne Gaudin[a], Véronique Ansan[a], Jean-Pierre Lorand[a], Sylvain Pont[b]

[a]*Laboratoire de Planétologie et Géodynamique à Nantes (LPG), Nantes Université, UMR 6112 CNRS, 2 rue de la Houssinière, BP92208, 44322 Nantes, France.*

[b] *Institut de Minéralogie, de Physique des Matériaux, et de Cosmochimie (IMPMC) - Sorbonne Université- Muséum National d'Histoire Naturelle, UPMC Université Paris 06, UMR CNRS 7590, IRD UMR 206, 61 rue Buffon, 75005 Paris, France.*

Keywords: Kaolinite, Al phosphate, REE, weathering, hydrothermal alteration, Armorican Massif

ABSTRACT

Several kaolinite occurrences of economic interest have been reported in Europe and are usually interpreted as resulting from weathering during the Paleogene tropical climate. However, a hydrothermal contribution is also recognized in some kaolinite occurrences. Such occurrences are common throughout the Hercynian Armorican Massif, where they are developed mostly on granitoids. The kaolin deposit of the Tertre Rouge pit, South Brittany (France), has been mined for the past 70 years. It is the only deposit developed from carbon-rich (~1% C) Ordovician schists affected by a low-grade metamorphic event during the late Hercynian orogeny. Herein, we report the results of a detailed field and petrological study combining optical microscopy with SEM investigation, XRD analyses, and ICP-OES and ICPMS geochemical data. A typical weathering profile was identified in the pit. It is marked from the bottom to the top by an increasing kaolinite volume (~45%) at the expense of muscovite/illite, a decreasing volume of chlorite and graphite, and numerous occurrences of Fe oxides/oxyhydroxides that replaced former pyrites or sulfates in veins. Despite this intense weathering, the analyzed Tertre Rouge schists preserved a black shale bulk chemical

composition characterized by lithophile trace elements contents at 2× to 5× the Upper Continental Crust composition. This was made possible by accessory minerals inherited from the parent rock, especially Al phosphates, namely florencite (Ce), which were systematically identified as the main concentrators of LREE and Sr. Their occurrence in the Tertre Rouge kaolinized schist confirms the regional Sr and P geochemical anomalies previously reported in the Paleozoic sedimentary formations in this area of the Armorican Massif. High temperature clay minerals, pyrophyllite (>270 °C) and nacrite/dickite (generally considered to be high-T kaolinite polymorphs), were also identified inside the weathered zone, filling millimeter-thick veinlets cutting across or lying parallel to the cleavage plane S of the schist. We ascribe this high-temperature clay mineral assemblage to a hydrothermal event related to the numerous documented evidences of Late Hercynian fluid circulations in Central/South Armorican tectonometamorphic domains. Hence, we strongly favor a two-stage formation for the Tertre Rouge kaolin deposit, including a minor hydrothermal contribution to weathering-related kaolinite.

1- INTRODUCTION

Numerous thick kaolinite-rich weathering profiles developed from various Paleozoic metamorphic rocks or granitoids have been reported in Europe (Fig. 1 and Table 1) and are usually thought to have formed during the Paleogene tropical climate (Dill, 2010, 2016, and references therein). However, superimposed hydrothermal and supergene alteration features have also been reported, for example in kaolin deposits associated with granites in France (e.g. Dudoignon et al., 1988) or with felsic volcanic rocks and metapelites in Spain (Clauer et al., 2015; Galan et al., 2016). Such kaolinite occurrences are also abundant throughout the Hercynian Armorican Massif, where they occur in sedimentary, metamorphic, and granitic rocks (e. g. Nicolas, 1956; Bellion, 1979; Boulvais et al., 2000; Estéoule-Choux, 1967, 1983;

Gaudin et al., 2015) (Fig. 2). Hydrogen and oxygen stable isotope compositions suggest a supergene origin for most of them (Boulvais et al., 2000; Gaudin et al., 2015). However, a minor hydrothermal contribution is also postulated for those industrial quality deposits that formed from granites, the largest ones being in Brittany (Plemet, Quessoy, Berrien, Ploemeur; Fig. 2). This is especially the case for the Ploemeur kaolin deposit in which Boulvais et al. (2000) identified a minor contribution of hydrothermal fluids in the vicinity of quartz veins. The Berrien deposit in the Huelgoat granite was ascribed to a post-magmatic hydrothermal event by Chauris (1984).

The Armorican Massif also comprises schist-hosted kaolinite deposits of a lesser size compared to the granite-hosted deposits (e.g. Estéoule-Choux, 1967; Bellion, 1979; Chauris, 1996; Boulvais et al., 2000). In this paper, we report a detailed investigation of the Tertre Rouge kaolin deposit near Chateaubriant, in southern Brittany, France, which has been worked since 1948. This deposit formed from Middle Ordovician schists of the "Angers-Traveusot" Formation (Fig. 2). In an earlier study, Nicolas (1956) suggested a supergene origin for this deposit. However, there is considerable evidence of Hercynian hydrothermal circulation leading to the formation of Pb-Sb-Au deposits all around this occurrence, such as those associated with Late Carboniferous diabase dikes crosscutting Ordovician schists in the northwest of Chateaubriant (Pochon et al., 2016, 2017, 2018), and as ore deposits within the Lower Ordovician named the "*Grès armoricain*" Formation in the Saint-Aubin-des-Châteaux pit (Gloaguen et al., 2007; Fig. 2), that are very close to the studied site. The degree to which such hydrothermal events contributed to the Tertre Rouge kaolin deposits is unknown.

This paper presents the results of a field study combined with a detailed investigation of the host rocks and the constituent minerals. Particular attention was paid to trace phases because kaolinite deposits frequently show REE-rich aluminum phosphates and sulfates of the alunite

group (APS) (e.g. Dill et al., 2010; Dill, 2016; Fig. 1, Table 1) and previous papers indicated P and REE geochemical anomalies and a great diversity of phosphates including Sc- and/or Sr-bearing species in the Lower Ordovician sandstones underlying the Tertre Rouge deposits (Moëlo et al., 2002) (Fig. 2). Phosphate-rich levels were also identified by Durand and Noblet (1986) and Dadet et al. (1987) within the Middle Ordovician schists in which is located the Tertre Rouge pit.

Our data allowed us to address some fundamental issues: (1) The origin and nature of the REE-bearing minerals detected within the schists, (2) the mineralogical reactions and the physical/chemical conditions (temperature, redox) associated with the kaolinization processes, and (3) the origin of the supergene and hypogene processes, with respect to geological processes that were recorded in the geological history of the Hercynian orogenesis.

2- GEOLOGICAL SETTING

The Tertre Rouge pit is located near the small town of Saint-Aubin-des-Châteaux, 10 km southwest from Chateaubriant in the central part of the Armorican Massif (Fig. 2a), a part of the Hercynian belt in the western part of France. The Armorican Massif comprises three main tectono-metamorphic domains (Northern, Central, and Southern Armorican Domains) separated by two main dextral crustal-scale shear zones (the North Armorican Shear Zone (NASZ) and the South Armorican Shear Zone (SASZ)), active between the Middle and the Late Carboniferous (Jégouzo, 1980; Le Corre et al., 1991; Gumiaux et al., 2004 ; Ballèvre et al., 2009; 2012).

The Central Armorican Domain is mostly composed of a Neo-Proterozoic pelitic basement covered unconformably by Paleozoic clastic sediments (Dadet et al., 1987; Trautmann et al., 1987; Dubreuil et al., 1988; Herrouin et al., 1989; Chantraine et al., 1996). The regional

Paleozoic sedimentary deposition was begun by the Lower Ordovician sandstones, called the *"Grès armoricain"* formation, which were deposited during an important marine transgression (Guillocheau and Rolet, 1982; Durand and Noblet, 1986). A near-shore sedimentary paleoenvironment comprising an internal platform, that was affected by storm activity, protected by barriers was suggested by Guillocheau and Rolet (1982). Above the "*Grès armoricain*" formation, the Middle Ordovician formation consists of homogeneous mudstone to siltstone, called the "Angers-Traveusot" formation, with some sandy and phosphate intercalations. During the Middle Ordovician, clayey sediments were deposited in a subsiding internal platform, yielding an up to 500-m thick, homogeneous mudstone to siltstone. Sandy and phosphate intercalations are interpreted as brief episodes of drying (Durand and Noblet, 1986; Dadet et al., 1987). The marine sandy to clayey environments prevailed up to the Middle Devonian. During the Upper Devonian, small limestone basins opened alongside the southern boundary of Central Armorican Domain, in a close relationship with the northern branch of the SASZ (e.g. St-Julien-de Vouvantes basin, south of Erbray, Fig. 2b).

In the Central Armorican Domain, all sedimentary rocks underwent tectonic deformation associated with anchizonal-greenschist metamorphism, leading to the Paleozoic folded schists that were formed during the Carboniferous Hercynian orogenesis (Le Corre et al., 1991). Regional N110°E trending folds (Fig. 2b) associated with an axial cleavage plane (S) and a sub-horizontal stretching lineation are linked to regional-scale ductile dextral simple shearing along the SASZ (Gapais and le Corre, 1980; Choukroune et al., 1983; Gumiaux et al., 2004). Syn-kinematic peraluminous crustal granite intrusions (340-330 Ma, Carron et al., 1994) were emplaced along the SASZ during Carboniferous dextral shear (Berthé et al., 1979; Vigneresse and Brun, 1983). In addition, ore mineralizations (e.g. Pb, Sb, Au, and Zn) are hosted by and crosscut late Proterozoic and Paleozoic formations, along the north branch of SASZ. This Late Carboniferous ore deposition was coeval with the emplacement of the Late Hercynian granites,

suggesting a genetic relationship between both events (Chauris and Marcoux, 1994; Brown and Dallmeyer, 1996; Bouchot et al., 2005; Gloaguen et al., 2007). At the end of Late Carboniferous, a network of N160°E trending fractures and faults crosscut oblique folds and granite intrusions (Gapais and Le Corre, 1980).

Since the end the Paleozoic era, the Armorican Massif underwent intense sub-tropical wet climatic conditions, favoring weathering and the formation of lateritic soils (e. g. Estéoule-Choux, 1983; Le Corre et al., 1991).

3- TERTRE ROUGE PIT

The Tertre Rouge pit located to the SE of Saint-Aubin-des-châteaux (Fig. 2b) has been working since 1948. Today the B.N.Z. company still extracts the kaolinized schist for the manufacture of firebricks. It is excavated into the Middle Ordovician slaty schists ("Calymene-bearing schists" in ancient geological maps) from the "Angers-Traveusot" formation located into the south limb of WNW-ESE trending anticlinal fold. The pit covers a surface of 20,000 m^2, with a mean depth of ~ 5 to 7 m (Fig. 2c). The pit face shows four superposed lithological levels (Table 2 and Fig. 3): A lowermost level (TRS-0) of greyish schist preserving sub-vertical (WNW-ESE/85°S) cleavage (S) with veinlets and nodules of iron oxides associated with centimetric thick quartz veins (Fig. 3a). Above this level, a ~4 m thick darker claystone schist level containing a few trilobite fossils (Dubreuil et al., 1988) (Figs. 3b-e) exists; this level was called "blue claystone" by Nicolas (1956) (TRS-1, TRS-2). This blue claystone level is separated from the underlying schists by an irregular surface. Although preserving a cleavage, the schist starts losing its cohesion while displaying a shiny brightness; the dark claystone schist is overlain by a ~50 cm thick bleached schist level, containing <1 cm in diameter iron oxide nodules (Fig. 3c, TRS-3). At the top, this level is limited by an erosion surface. The uppermost

~1.5- to 2-m thick yellow/orange level contains cobbles of iron-bearing sandstones and iron-rich massive to granular materials embedded in a yellow/orange/grey argillaceous matrix (Figs. 3b, c). This latter level, not studied here, corresponds to a debris-flow deposit above the erosion surface. Incipient alteration features may be observed throughout the outcrop down to the lowermost greyish schist, such as reddish materials deposited onto discontinuity planes or in filling millimetric veins cross-cutting the cleavage S.

Irrespective of the depth, the outcrops show numerous millimeter thick veins/veinlets filled with white, yellow, or orange argillaceous materials, secant or parallel to the cleavage (Figs. 3d–i). Moreover, thicker centimetric quartz veins also occur locally inside the basal schist level.

4. ANALYTICAL METHODS

Fourteen samples collected from the three schist levels defined in section 3 (samples TRS- 0, 1, 2, and 3) and within the different veins (TRV- 1, 2, and 3) were studied (Table 2, Figs 1c, and 2). Polished thin sections were prepared after drying and repeated impregnation under vacuum with an unsaturated polyester resin with acetone. The thin sections were investigated with an Olympus BH2 optical microscope operating in transmitted and reflected light.

Major minerals were identified with room temperature bulk-rock X-Ray Diffraction (XRD) analyses conducted at the “Institut des Matériaux de Nantes-IMN”, using a Brüker “D8 Advance” powder diffractometer operated in Bragg-Brentano geometry with a Cu anode sealed X-ray tube and a focusing Ge(111) primary monochromator (selecting the Cu $K\alpha_1$ radiation ; λ = 1.540598 Å). We used a 1-D silicon-strip position sensitive detector (“LynxEye” detector) with an active area of 3.7° 2Θ (goniometer radius: 217.5 mm). This type of detector prevents the XRD pattern interpretation of the pattern for °2Θ values lower than 4°. The XRD patterns

were obtained on bulk powders (XRPD) and on air-dried, ethylene glycol-saturated (EG) and heated (550 °C during 12 h) oriented clay fractions. For bulk powders, measurements were performed between 3.5 and 70 °2Θ with steps of 0.0157° and a counting time per step of 0.8 s. Measurements of the oriented clay fractions were done between 3.5 and 33 °2Θ with steps of 0.0157° and a counting time per step of 1.7 s. The <2 mm clay fractions were extracted by a sedimentation procedure. For this procedure, deionized water was used and a dispersing agent (sodium hexametaphosphate) was added to prevent the flocculation of clay particles.

The clay minerals were also studied for their morphology, using a JEOL JSM 5300 SEM at the IMN, operating at an acceleration voltage of 20 kV. Minor and trace minerals were located with the same SEM facility using back scattered electron (BSE) and X-Ray scanning maps. They were investigated in more detail on two polished thin sections of the sample TRS-0 with a Tescan VEGA II LSU SEM equipped with a silicon drift (Bruker) Energy Dispersive Spectrometer (EDS) (Muséum National d'Histoire Naturelle-MNHN, Paris, France). Each section was investigated with manual scans in the BSE mode.

The bulk-rock chemical analyses were performed in a commercial lab, at the “Service d’analyse des roches et minéraux, SARM”; Centre de Recherches Pétrographiques et Géochimiques (CRPG), Nancy (France). Briefly, for each of the 6 analyzed samples, 1 g of rock powder was attacked with an alkaline fusion procedure ($LiBO_3$) followed by acid dissolution (HNO_3). This procedure enables the dissolution of refractory minerals such as zircon and rutile. Major elements were measured by inductively coupled plasma-optical emission spectrometry (ICP-OES, iCap6500 ThermoFisher). Lithophile trace element contents (Large ions lithophile elements, -LILE, Rare Earth Elements-REE, High Field Strength Elements-HFSE and transition elements) were obtained by inductively coupled plasma-mass spectrometry (ICP-MS, iCapQ ThermoFisher).

5. MINERALOGY

5.1. Optical microscopy

Under the microscope, the thin sections of schist samples (TRS-0 to TRS-3) show a fine-grained carbon-bearing muscovite-quartz assemblage defining a porphyroclastic texture (Figs. 4 and 5a). The cleavage is outlined by a preferential orientation of clastic muscovite flakes. Porphyroclasts of quartz/mica of 100–300 µm show pressure shadows (Fig. 4a). The minor minerals identified by transmitted light optical microscopy are as follows: Rutile (up to 10 µm in diameter) sometimes aligned within the cleavage plane S, Fe oxyhydroxides sometimes preserving euhedral crystal faces (former pyrite, see below), zircon and phosphate minerals misidentified as apatite under the microscope but identified as a Light Rare Earth Elements-rich aluminum phosphate (florencite) by XRD and SEM analyses (see below). Contorted graphite flakes, that were 10-µm thick, were identified in reflected light in the carbon-rich layers. As suggested by field observations, the dark grey altered schist samples (TRS-1, 2) are strongly enriched in blackish carbonaceous matter which obscures their petrography (Figs. 4b and c). By contrast, large domains of the bleached schists at the top of the outcrop (TRS-3) may be carbon-free (Fig. 4d).

Incipient alteration features within the TRS-0 schists are marked by the abnormal polarizing tints of muscovite under crossed polarizer transmitted light, corresponding to the first order abnormal interference colors of kaolinite (see XRD data below). The replacement of muscovite by kaolinite begins from crystal boundaries or along (001) cleavage planes which appear exfoliated (Figs. 5a, b). Moreover, some micro-veins of phyllosilicates showing the same 1st order polarization tints of kaolinite crosscut the cleavage plane S. Numerous reddish iron oxy-hydroxide phases are observed in filling veins or as micrometric spherules inside the schist (Fig. 5a).

Sample TRS-1, collected in the upper section, shows a vein network secant to cleavage S (TRV-1) (Figs. 4b and c). The vein-filling mineral is pyrophyllite, which can be easily distinguished from the kaolin polytypes by its 2nd order polarizing tints. Pyrophyllite elongated flakes are stacked in such veins; however, the same orientation as the cleavage plan S in the host rock is preserved (Figs. 4c and 5c-g). Sub-parallel quartz grains or kaolin-type phyllosilicates (confirmed by SEM, see below) are locally intercalated with pyrophyllite (Figs. 5e, f, and 6a). Further identification of kaolin polytypes under the microscope is difficult, as nacrite, dickite, and kaolinite all have very similar optical properties. However, the pyrophyllite is replaced by large phyllosilicates crystals of several tens of micrometers with low birefringence polarizing tints that could be interpreted as highly crystalline euhedral nacrite/dickite platelets (see XRD, Table 2, and Figs. 5f, g, and 6b). These platelets start crystallizing from the grain boundaries of pyrophyllite crystals or within their loosely cleaved (001) crystal planes (Figs 5f and g). They may also occur as newly formed crystals inside vugs (Fig. 5h). In another generation of thin micro-veins cutting across pyrophyllite crystals (Fig. 5c), phyllosilicates showing low birefringence tints are observed, but with smaller sizes (<10 µm) and with more irregular and diffuse shapes, suggesting a lower crystallinity compared to "dickite/nacrite". These phyllosilicate particles could be interpreted as being kaolinite. Such small-size phyllosilicates may also replace the pyrophyllite crystals generating clustered randomly oriented particles (Figs. 5d and e). Clusters of small quartz grains may also be present (Fig. 5d).

5.2. XRD data

According to the bulk-rock XRD data (Table 2 and Fig. 7), the TRS-0 sample, which was collected at the bottom of the outcrop, is dominated by quartz and mica, while significant amounts of chlorite (14.17 Å, (001); 4.71 Å, (003)) and kaolinite (7.15 Å, (001)) are detected

by XRD (Fig. 7a) (Note the overlap of the diffraction peaks at 7.15 Å of the kaolinite and that of chlorite at 7.08 Å (002), Fig. 8a). If normalized to the intensity of the same diffraction peak in the mica, the intensity of the (001) reflection peaks of kaolinite at 7.15 Å is higher in the TRS-1, 2, and 3 samples than in the TRS-0 sample (Fig. 8a). Clearly such a variation indicates an increasingly modal abundance of kaolinite in the TRS-1, 2, 3 samples; this agrees well with the micro-textural evidence of the replacement of muscovite by kaolinite as discussed above (Figs. 5a, b). By contrast, chlorite disappears totally in the dark and bleached schists (TRS-1, 2, 3) that show negligible amounts of this mineral (e.g. TRS-1d; Table 2). The bleached schist (TRS-3) at the top of the profile displays no significant mineralogical change compared to TRS-1, especially regarding kaolinite abundance. Its whitish color only results from a decrease in carbon content and not due to different phyllosilicate modal proportions. XRD also identified several minor minerals inside the studied schists, i.e. rutile, florencite, and pyrophyllite. Florencite was detected due to its main diffraction peaks at 5.69 Å, 3.50 Å, and 2.95 Å corresponding to (101), (110), and (113) reflections, respectively (Fig. 7d). Rutile and florencite occur throughout the three levels defined in (3) (Table 2, Fig. 7a). Pyrophyllite was also detected but is lacking from bleached schist TRS-3.

XRD identifies the white minerals extracted from the veins TRV-1, TRV-1d as pyrophyllite (9.2 Å, (001)), kaolinite, and quartz, in excellent agreement with our observations under the microscope (Table 2 and Figs. 5c-h, 7b and c). Moreover, a closer look at the XRD patterns in the 34–40 °2Θ angular domain allows a significant amount of nacrite and dickite (kaolin group) to be detected in both samples (Fig. 7c). Nacrite is easily identified by its main peaks at 2.44 Å, 2.43 Å, 2.41 Å and 2.40 Å corresponding to (-314), (022), (310) and (006) reflections, respectively; dickite displays the diagnostic peak at 2.32 Å ((132), (20-4)) (Fig. 7c). Therefore, the diffraction peak observed at 7.15 Å actually corresponds to both the kaolinite, nacrite and dickite basal reflections (Fig. 7b). Small amounts of mica, chlorite, and smectite

minerals also occur in these samples. Almost pure nacrite/dickite was identified in the two veins, TRV-2a and TRV-2b (Fig. 7b). TRV-2a consists mainly of nacrite with minor amount of dickite and quartz. TRV-2b is a dickite vein containing small amounts of nacrite, goethite, hematite, and quartz (Figs. 7b and c and Table 2). No evidence of kaolinite was found in these two samples.

A good indicator of the crystallinity index of kaolin-group minerals is the full width at half maximum (FWHM) values measured for the basal diffraction peaks at 7.15 Å (Fig. 8b). This parameter decreases with the increase in the nacrite/dickite abundance in veins, with values between 0.26° and 0.44 °2Θ for the kaolinite-rich schists (TRS-1, TRS-2, and TRS-3), 0.16–0.19 °2Θ for the kaolinite/nacrite/dickite-rich veins (TRV-1a and TRV-1b) and 0.10–0.11 °2Θ for the nacrite/dickite veins (TRV-2a and TRV-2b). Such a decrease in the FWHM values is predicted by the higher crystallinity index of nacrite/dickite minerals compared to kaolinite (Brindley and Brown, 1980). Moreover, the d(001) value of the mica/illite is 9.98 Å and its FWHM value is 0.2 °2Θ. Based on the terminology proposed by Lanson et al. (1998), these values are assigned to a well crystallized illite or mica (WCI).

In addition, one yellow vein (TRV-2c) collected within the dark grey unit was analyzed with XRD that identified jarosite ($KFe^{3+}_3(SO_4)_2(OH)_6$) (Fig. 2f) as the only major mineral in that vein (Table 2).

5.3. SEM

SEM pictures provide further evidence for the highly crystalline nacrite/dickite occurrences within the veins TRV-2a and TRV-2b, in line with XRD data (Figs 6c–f). A broad range of crystal shapes, including pseudohexagonal or elongated morphologies and booklets have been recognized (Figs. 6c, e, and f). Their dimensions are relatively uniform, about 10 µm in diameter for the pseudohexagonal platelets and about 30 µm for the elongated ones with a

quite constant thickness of about 5 µm. Thicker crystals (up to 60 µm; Fig. 6d) are uncommon. Some crystal surfaces exhibit dissolution pits and micrometric iron-rich spherules that EDS spectra identify as Fe (oxy) hydroxides (likely goethite) and/or hematite by (Figs. 6e and f), in agreement with the XRD data (Table 2).

Minor and trace phases were studied in greater detail in the TRS-0c sample, the closest to the bottom level exposed in the Tertre Rouge pit. Florencite was localized owing to BSE maps and X-ray maps of P, Ca, and Al (Fig. 9). These maps demonstrate that florencite is widely disseminated in the thin section. Further, the maps also detected trace amounts of calcium sulfate (<5-µm large). A manual scan in the BSE mode was performed over one thin section (representing c.a. 4 cm^2) to get high-magnification pictures of florencite (Fig. 10). This mineral commonly occurs as amygdaloid fine-grained/framboid aggregates, and less frequently as fractured monocrystalline grains. In the latter case (Fig. 10a), the florencite crystals do not exceed 5×7 µm in maximal dimensions and display ragged grain boundaries. They are outlined by muscovite or its replacement products (kaolinite) forming ovoid shadow pressures (Figs. 10a and b). This type of microtexture indicates tectonic rotation of the florencite crystals within cleavage S. Such a rotation coeval with granulation is also obvious regarding the framboid aggregates that may be up to 20 µm in length for a thickness of only 3–4 µm (Fig. 10c). Calcium, Sr, and trace amounts of Th, were systematically detected in the 11 florencite grains analyzed with EDS, in addition to the major elements Al, P and Light Rare Earth Elements (LREE; La, Nd, Ce) (Fig. 10d). One semi-quantitative SEM-EDX analysis with external calibration standards yields the following structural formulae of florencite (Ce) (calculated on the basis of 11 oxygens) -$La_{0.15}Nd_{0.13}Ce_{0.28}Sr_{0.24}Fe_{0.05}Ca_{0.17}Al_{3.32}$ $(P_{1.87}O_8)$ $(OH)_6$ (Fig. 10d). Its slight Al excess is correlated with Si (not shown here) indicating contamination of the analysis by mica and/or kaolinite.

Several other trace minerals were detected during the manual scan on TRS-0c, in addition to florencite and rutile already documented by the bulk-rock XRD data. These are ordered by decreasing order of abundance iron oxyhydroxides, zircon, xenotime, monazite, ilmenite, and barite (Fig. 11). Iron oxyhydroxides are micrometric cubic crystals (×10 µm) that replace pyrite crystals or anhedral ovoid/framboid aggregates (Fig. 11). Their EDS spectra systematically display a sulfur peak, suggesting a sulfide precursor. Zircon occurs as rounded abraded grains or quadrangular shapes with fuzzy crystalline faces, up to 20 × 10 µm in the largest dimension. Two different zircon chemistries were recognized from the EDS spectra: one is pure $ZrSiO_4$ and the other systematically contains Ca, Sc, and Th as major elements. Xenotime occurs as corroded grains up to 30 µm in diameter. Yttrium and heavy rare earth elements (HREE), Dy, Gd, and Er, were detected with the SEM. Monazite grains are smaller (<3 µm), rounded to prismatic crystals containing LREE (Ce, La, and Nd) and Th in addition to P and O.

6. BULK-ROCK MAJOR AND TRACE ELEMENTS.

Six representative samples were analyzed for major and trace elements, three schists (TRS-0b and TRS-0c; TRS-1d) and the three clay veins (TRV-1, TRV-2a, and TRV-2b) (Tables 3, 4). Their major element contents strongly reflect the changes documented above in their major mineral assemblages. Compared to TRS-0b and TRS-0c, TRS1-d is poorer in SiO_2, K_2O, and MgO and richer in Al_2O_3, while showing a higher Loss on Ignition (LOI) value. This trend hightlights the increasing amount of kaolinite and decreasing amount of mica/illite and chlorite observed in TRS1-d by XRD. By contrast, other minor element contents (C, Na, Ca, Ti, and P) do not show any variation. The total carbon contents are uniformly low (<1 wt.%) in agreement with the scarcity of graphite under the microscope. The constant contents of TiO_2 and P_2O_5 are

accounted for by ubiquitous occurrences of rutile and florencite, respectively, based on XRD data. These two elements can be balanced with ca 1% by weight of rutile and 1% of florencite if both mineral abundances are calculated from their pure end-member compositions (Florencite: (La, Ce, Nd)$(PO_4)_2(OH)_6$; Rutile: TiO_2). The Fe_2O_3 content comes from the various occurrences of Fe oxyhydroxides observed with SEM and optical microscopy within the Tertre Rouge schists.

The three clay veins show a similar relationship between their mineral assemblages and their major element compositions. The veins TRV-2a and TRV-2b match the bulk-composition of kaolin-group minerals very well, in agreement with their observed mineralogy. Their trace amounts of TiO_2 and P_2O_5 (bdl TRV-2b) may reside in highly accessory rutile and florencite while Na_2O (bdl TRV-2b) and K_2O are linked with trace amounts of illite/mica. MgO is close to detection limits (bdl TRV-2b) in line with the absence of chlorite. TRV-1d is higher in SiO_2 (quartz, pyrophyllite), K_2O (mica) and MgO (chlorite) and lower in Al_2O_3 and has a lower LOI value, because of a lower modal proportion of clay minerals compared to TRV-2a and TRV-2b. P_2O_5 and TiO_2 contents are below detection limits (Table 3), suggesting that neither florencite nor other phosphates or rutile are present in these veins. Note that Ca was systematically detected regardless of the contents of P_2O_5. It can be inferred from this observation that the Ca sulfates found with SEM X-ray maps (Fig. 10) are ubiquitous in the Tertre Rouge clay veins.

The same straightforward relationship between the bulk-rock geochemistry and the mineralogy also holds true for the trace elements (Table 4, Fig. 12). All of the three analyzed schists show reproducible lithophile trace elements contents of the mudstones and the organic matter-bearing shales at 2× to 5× the Upper Continental Crust composition (Rudnick and Gao, 2014; Fig. 12). Their normalized patterns display strong positive anomalies of Be, Cu, and Sr coupled with a slight negative anomaly of HFSE (Zr Hf) and transition elements Ni and Co. All

of these anomalies (except Be) can be accounted for by minor phases such as Fe sulfides for Cu and florencite accumulation for Sr, while the Zr-Hf deficiency is related to zircon (no evidence of a zircon placer), and the negative Ni and Co anomaly may reflect the absence of mafic minerals. In additional possible binary correlations within the bulk-rock data were calculated (Table S1). If close to 1, their coefficients correlations with the major index elements (TiO_2, K_2O, P_2O_5) indicate the major mineral concentrator for each element, in addition to SEM EDS analyses of Figs 9 and 10. It can be deduced that LILE (Ba, Rb, and Cs) and Pb are preferentially hosted in mica/illite. Sr-bearing florencite is the main concentrator for Sr, Th, and LREE, with LREE+MREE and Th being also hosted in monazite (SEM EDS data). Xenotime controls Y and HREE. The homogeneous distribution of florencite in all of the three analyzed schists perfectly accounts for the very flat and highly reproducible LREE segment in the crust-normalized pattern of Fig. 12. It also explains the coherent geochemical behavior of P, V, and Cr; all three elements may replace PO_4 in the anionic group of phosphates (see Chang et al., 1997). By contrast, the variability of MREE and HREE likely reflects more complex distribution patterns between two trace phases (xenotime + zircon). Zircon is the main concentrator of Sc, Zr, Hf, and U while rutile carries the budget of Nb, Ta, and W. Note that multiple positive correlations between chalcophile elements Cu-Co-Zn and Sn, yet no Cu-Zn sulfides were detected with the SEM. The good positive correlation between Sb and Mo is characteristic of euxinic shale sediments (residual altered pyrite) (Samalens et al., 2017; Coveney and Pasava, 2004; Large et al., 2007).

Our qualitative assessment of the trace element mineral carriers is validated by the analyses of the three clay veins (Table 4, Fig. 12). Compared to the schists, all the veins are strongly depleted in LILE (Cs, Rb, Ba, Sr, Th, U, and LREE) and HFSE (Zr, Hf, Nb, and Ta); this agrees with the near 0 modal abundance of mica, florencite, and rutile in those veins. Their HFSE contents positively correlate with TiO_2, while LREE correlate with P_2O_5, thus outlining

the part played by rutile and florencite in the trace element budget. A more complex behavior can be inferred from Fig. 12 for the transition elements (Sc, V, and Cr) Y and HREE that do not show systematic concentration changes with respect to the schists. Their behavior likely reflects a multimineral partitioning effect and a stronger preference for the crystalline structure of clay minerals (cf Linnen et al., 2014).

7. DISCUSSION

Similar to the several kaolin deposits described thus far, the Tertre Rouge deposit shows evidence of a polygenic formation process of clay minerals, such as (i) the pervasive replacement of the schists by kaolinite and other secondary minerals (Fe oxyhydroxides); (ii) the crystallization of nacrite-dickite-pyrophyllite inside veins/veinlets that were unrelated to the pervasive pit scale formation process of kaolinite. Both processes involved a peculiar carbon-rich schist parent material characterized by aluminum phosphates (namely Sr- and Ca-bearing florencite (Ce)). This protolith, ascribed to Middle Ordovician continental platforms, will be discussed first, before addressing the timing and petrogenesis of clay formation.

7.1 Florencite-bearing Ordovician sedimentary parent rock composition

The bulk-rock analyses of the Tertre Rouge schists are indicative of an upper crust mudstone/shale composition characterized by a two-fold metal enrichment (As, Be, Bi, Cr, Ga, Cu, In, Pb, Sc, Sn, Ta, Th, V, P, and Ti) compared with the estimate made by Rudnick and Gao (2014). With respect to most predominant and trace elements, the mudstone composition sampled in the Tertre Rouge schists is similar to that of quoted averages for post-Archean shales (Wedepohl, 1971). Transition and non-transition metal contents agree reasonably well with worldwide average shale compositions (Johnson et al., 2017). Several elements, however, do

not exhibit a very good fit. First row transition metals Cr, V, and Ni are slightly enriched, reflecting phyllosilicate/chlorite contents. The high Sr concentration (up to 1470 ppm) compared with the upper crustal mudstone average (115 ppm; Taylor and Mc Lennan, 1985) is a regional benchmark previously noted by Chauvel and Pan (1965), Moëlo et al. (2002), and Gloaguen et al. (2007). As it is not correlated with CaO enhancements, this anomaly cannot result from diagenetic/biogenetic carbonates. The Sr-sink identified using SEM is the Al phosphate florencite, which also accounts for elevated Ce, P, and Th levels in the Tertre Rouge schists compared with post-Archean shales. In addition to the geochemical features discussed earlier, the Tertre Rouge schists exhibit a mineralogy that is consistent with euxinic epicontinental reducing shales; organic matter compounds are now present as graphite and other unstudied oil organics that amount to 0.9 wt.% C. The schists also host framboidal and cubic pyrite now replaced by FeOOH-like minerals, the most common pyrite textures documented in carbonaceous sedimentary rocks. These framboidal and minute-euhedral matrix pyrite types are formed from ambient marine waters at or near the sediment–water interface (Berner et al., 2013). Compared with metalliferous shales (e.g. Wedepohl, 1971; Taylor and McLennan, 1985), however, the low Mo level (<0.6 ppm) is noteworthy. The metals in black shales are mainly in the forms of sulfides and complexes incorporated with organic matter (OM) (Brumsack, 2006; Holland, H.D., 1979; Wedehpohl, 1971). OM in metalliferous shales tends to decompose under oxidizing conditions generated by supergene weathering, and it break downs at a low pH owing to the leaching of sulfides. The subsequent release of heavy metals and erratic variations in metal contents (Ni, Cu) may have occurred from these Tertre Rouge shales via the superimposed weathering profile that also altered the pyrite. The Cu-bearing fractions in shales and cherts are sulfides and OM, and sulfides react faster with O_2 than OM does, thus leading to metal leaching (Tribovillard et al., 2006).

As shown by the calculated correlation coefficients listed in Table S1, the REE (at least

Light Rare Earth Elements), P, Th, and Sr budget is clearly controlled by accessory phosphates (namely florencite; predominant over monazite and xenotime-Y). Florencite is a phosphate member of a phosphate subgroup of the alunite supergroup of minerals having the general formula $AB_3(XO_4)_2(OH)_6$, where the A-site is filled with Ce, La, and Nd; the B-site with Al; and the X-site with P (Bayliss et al., 2010). The structure of florencite also accommodates varying amounts of Ca^{2+}, Pb^{2+}, Hg^{2+}, K^{+}, Ba^{2+}, Sr^{2+}, Rb^{+} (in A-site), Fe^{3+}, Cu^{2+}, Zn^{2+}, Sn^{2+}, V^{3+}, Cr^{3+}, and Ga^{3+} (in B-site) (Dill, 2001; Gaboreau et al., 2005; Repina et al., 2011). The Tertre Rouge florencites are generally too fine-grained to provide reliable in-situ compositions; only one particle allowed us to obtain its structural formulae: - $La_{0.15}Nd_{0.13}Ce_{0.28}Sr_{0.24}Fe_{0.05}Ca_{0.17}Al_{3.32}$ $(P_{1.87}O_8)$ $(OH)_6$ (calculated on the basis of 11 oxygen atoms). Their EDS spectra systematically detected Ca and Sr, indicating solid solutions toward goyazite and crandallite, which are two other types of aluminum phosphate (Fig. 10). Thorium was detected in half of the EDS spectra as well, suggesting the substitution of $2REE^{3+}$ by Ca^{2+} + Th^{4+}. Sulfur was also detected, suggesting a significant solution toward sulfates (a property of Al phosphates in the APS association, see Dill, 2001 and reference therein).

APS minerals of the goyazite ($SrA1_3(PO_4)_2(OH)_5$-H_20) group, including florencite-Ce, have been identified in a number of Australian coals, as well as in kaolinite claystones (tonsteins) associated with coal seams in New South Wales (Ward et al., 1996). These phosphates typically represent a range of solid solutions containing goyazite, gorceixite ($BaAI_3(PO_4)_2(OH)_6 \cdot H_20$), crandallite ($CaA1_3(PO_4)_2(OH)_5 \cdot H_20$), and florencite ((La, Ce, Nd)$Al_3(PO_4)_2(OH)_6$). They may be authigenic in shales and sandstone (e.g. early diagenetic REE, Al phosphate minerals in marine sandstones are a major sink for oceanic biogenic phosphorus (Pouliot and Hoffmann, 1981; Rasmussen, 1996 and references therein)). They may be a weathering product in argillized igneous rocks, resulting from pervasive chemical alteration of primary phosphates (Nriagu and Moore, 1984; Schwab et al., 1989) and coexisting

with various Al phosphates formed in close association with or intimately intergrown with goethite and kaolinite. Zou et al. (2016) reported florencite along with zircon and pyrite in the kaolinite matrix of an alteration profile involving sandstone and mudstone hosted by the Permian tuff (China). Gypsum occurs in radiating forms, while jarosite occurs as fracture-fillings, indicating a weathering product of pyrite. Banfield and Eggleton (1989) described the extensive supergene replacement of apatite by florencite-(La) and florencite-(Ce), along with euhedral hydrous Ce phosphate (rhabdophane) in Bemboka granodiorite (southern New South Wales, Australia). Deeply weathered plagioclase (replaced by kaolinite and halloysite) and K-feldspar (replaced by kaolinite) provided the Al that entered the florencite. Dill et al. (1997) reported the formation of florencite from supergene alteration in a western Peru kaolin deposit developed from rhyolitic rocks. Florencite is also commonly cited as a detrital mineral in various placer deposits (e.g. Gabon; Janeycky and Ewing, 1996). Florencite was first reported in France in heavy mineral concentrates from Cambro-Ordovician mudstone/sandstone sediments from the northern Armorican Massif (Devisme et al., 1968).

According to textural microcriteria, the Tertre Rouge florencite is unrelated to the weathering profile that kaolinized the Tertre Rouge schists. It is present from the bottom to the top of this profile and shows no preferential location inside the kaolinite sites. The shadow pressure around florencite ellipsoidal grains provides evidence for ante-schistosity and tectonic rotation toward the cleavage plan. Single crystals were granulated during this tectonic rotation, resulting in fine polycrystalline ellipsoidal grains. Taken as a whole, the florencite morphologies were deeply modified by the Late Hercynian deformation that generated the cleavage and low-grade metamorphism. Hence, it predates the Hercynian deformation, being most likely inherited from the original Ordovician mudstones (see Dabard et al., 2007). Whether it was authigenic, diagenetic, or of a detrital origin in those mudstones is difficult to determine from the available data. Rutile, zircon, and monazite, which are accessory minerals in the Tertre

Rouge schists, are common detrital minerals in Ordovician sedimentary formations, whether sandstones or mudstones, in the Armorican Massif (e.g. Donnot et al., 1973; Faure et al., 2008). Late Proterozoic granitoids are usually inferred to be the source rocks of these heavy minerals. The same weathering sequence of apatite and primary Al-silicates as the one documented in the literature (e.g. Banfield and Eggleton, 1989) could have generated florencite. An Apatite precursor could explain the reason for Ca being systematically detected in the Tertre Rouge florencite. Another source of fine-grained rutile, zircon, and monazite—having similar granulometry as the florencite documented in our study—are Late Proterozoic Brioverian schists (Ballèvre et al., 2012). Detrital florencite could be responsible for the strong positive Sr anomaly that characterizes the upper crust normalized trace element patterns of the Tertre Rouge schists (Fig. 12).

However, there exists as much evidence suggesting that florencite could be an authigenic diagenetic mineral APS. Because millimeter-sized crystals are common authigenic constituents of pyritic and phosphatic Precambrian black shales (e.g. Pouliot and Hoffmann, 1981). Al-bearing phosphates generally nucleate shortly after burial within the sulfate reduction zone, from bacterial decomposition of organic matter (Dill, 2001 and reference therein). In the original mudstones, REE are hosted in clay minerals and must be desorbed to provide the required REE content to Al phosphates. For crystallization, florencite requires either an Al sink that can be an Al-rich primary clay mineral during diagenesis, or a detrital feldspar/chlorite. Phosphatization of authigenic REE exhibits better agreement with the highly reproducible, nearly flat crust-normalized REE patterns of the Tertre Rouge schists, as well as with the widespread dissemination of florencite at the thin-section scale. Ordovician mudstones/sandstones collected from the southern area of the Central Armorican Domain display a regional-scale distribution of P and Sr minerals. Sr-rich apatite is a common component in the Saint-Aubin-des-Châteaux organic-rich ironstones (Chauvel and Phan, 1965;

Gloaguen et al., 2007). Several Middle Ordovician schist localities over the Chateaubriant-Grand Fougeray area exhibit a P anomaly in nodular monazite (Donnot et al., 1973) (Fig. 2). This phosphate is abundant in heavy mineral concentrates from the original bedrocks identified as the basement of the Calymene-bearing nodular black schists analogous to the Tertre Rouge schists. Donnot et al. (1973) provided mineralogical evidence that monazite was authigenic, not detrital, because it shows inclusions from all schist minerals. They suggested that hydrous Ce phosphate gel originated from the mudstones of the Ordovician sea enriched in P, Sr, and Ce, before undergoing diagenesis, which led to monazite nodules. Notably, nearly identical grey Ce-rich nodular monazite was also identified in the Stavelot massif (Belgium), in black terrigenous pyritic sequences of Cambrian quartzite schist, similar to the Tertre Rouge schists (Burnott et al., 1989). Another example of phosphatization of detrital minerals was provided by Möelo et al. (2002), who documented Sc phosphate (pretulite) and xenotime-(Y) as epitactic overgrowths on detrital zircon crystals in the Saint-Aubin-des-Châteaux Lower Ordovician ironstones (Chauvel, 1974). Finally, the original discovery in the Normandy and Maine-et-Loire Cambro-Ordovician mudstone/sandstone sediments (Devisme et al., 1968) shows evidence of the widespread formation of florencite in such sedimentary rocks in the Armorican Massif. The local geochemical factors that determined whether it was apatite, monazite, or an APS-group mineral that crystallized are not clear. The local pH at the time of precipitation may have played a part because apatite is usually only precipitated in neutral to alkaline conditions. Aluminum phosphate minerals are less soluble in acids than apatite is, and are indeed common in present-day soil deposits. Their formation may also have been related to the presence of available alumina (Ward et al., 1996).

Regardless of its actual origin (authigenic or detrital), once formed, florencite is difficult to be destroyed by metamorphism. Indeed, it was reported to exist in amphibolite-grade conditions (560 °C and up to 13 kbar (Nagy et al., 2002)), well beyond the anchizonal/lower

greenschist facies conditions inferred for the Tertre Rouge schists (Ballèvre et al., 2012 and references therein). The graphite paleo-temperatures reported by Donnot et al. (1973) for these rocks are only 250–300 °C, which are well within the stability field of florencite.

7.2 Evidence for weathering profile inside the Tertre Rouge deposit

There exist numerous lines of evidence supporting a supergene alteration process in the pervasive formation of kaolinite and associated secondary minerals in the Tertre Rouge pit. The XRD data indicate a sharp increase in the modal abundance of the kaolinite in the upper units (samples TRS- 1, 2, 3), compared with TRS-0; this suggests an alteration progressing from the paleo surface. Notably, however, the samples collected from the basement of the Tertre Rouge pit do not correspond to the frontline of this putative weathering profile, because the sample TRS-0 from the bottom unit contains approximately 45% kaolinite. This bottom-to-top change from 2:1 phyllosilicate (mica) to 1:1 phyllosilicate (kaolinite) was accompanied by leaching of Si and K by meteoric waters and a relative increase in aluminum concentration, as shown by the bulk-rock analyses (Table 3). Moreover, such a higher degree of alteration in the upper units is also shown by the following: (1) The higher plasticity of the schists in the units TRS 1, 2, 3, reflecting their higher clay modal contents; (2) The near-0 chlorite modal content, which is consistent with its instability under weathering conditions (e. g. Gaudin et al., 2015). Chlorite was likely responsible for the Mg losses observed in the upper units (Tables 2 and 3); (3) The oxidation and leaching of carbon in the bleached unit at the top of the profile; (4) Numerous reddish iron-rich veins that occur parallel or secant to the S cleavage plane, along with a wealth of reddish iron-rich spherules that are also observed to be disseminated within the schist; (5) Pyrite cubes pseudomorphosed by Fe oxyhydroxides; (6) Sulfate veins (jarosite) and disseminated gypsum. The latter oxidized phase assemblage suggests the existence of redox conditions of near-surface environments. Notably, the supergene origin of the kaolinization in the Tertre Rouge deposit appears coherent with the stable oxygen and hydrogen isotopic data

reported by Boulvais et al. (2000) for the former Croix-des-Landelles kaolin deposit, located near the Tertre Rouge site and also developed from Ordovician schists (Fig. 2).

Interestingly, the alteration of mica into kaolinite occurred in the Tertre Rouge schists without crystallization of intermediate mixed-layer minerals (MLM), which could not be detected using XRD, both in bulk samples and in <2-µm fractions. Such intermediate phyllosilicates have, however, been commonly reported in studies describing the transformation of the end-members of layer silicates, especially in weathering environments. For example, the weathering profile superimposed on the Penestin micaschists (Brittany, France; Fig. 2) produced the following alteration sequence: Mica (illite-like) → Illite/Vermiculite MLM → Vermiculite → V/K MLM → kaolinite (Gaudin et al., 2015). Han et al. (2014) reported a similar sequence of pedogenetic alteration of illite in red sediments from subtropical China. Interstratified mica/vermiculite has also been found in soil clay fractions from the upper horizons of podzolic soils (Churchman, 1978, 1980; Wilson et al., 1984). This mineralogical evolution with MLM intermediate phases is commonly reported in cases of partial leaching of Si and K during the weathering of mica (Millot, 1964; Wilson, 1999). Aspandiar and Eggleton (2002) suggested that interstratified products preferentially form during weathering of layer silicates in environments where pore-fluid space is limited; consequently, the solution and ionic transport pathways are restricted, and Si and K undergo moderate leaching.

For the Tertre Rouge pit, the lack of such interstratified phases could be explained by the advanced stage of alteration of the samples observed in this study; as suggested before, even for TRS-0, the samples collected from the bottom of the pit contain 45% kaolinite (vol.%). The MLMs could have formed during incipient weathering processes close to the unexposed bedrock levels in the Tertre Rouge pit. Moderate leaching of Si and K is expected at this level because of the confined medium due to limited pore-fluid spaces. Alternatively, the carbon-rich

environment of the Tertre Rouge schists, together with the possibly humic components, yielded acidic environments that resulted in the quicker dissolution of mica and the rapid leaching of Si and K (refer to the pH dependence of the dissolution kinetics of the muscovite used in room-temperature experiments performed by Kalinowski and Schweda (1996)).

During the weathering, the REE-bearing florencite appears well-preserved (Table 2). As previously mentioned, florencite is a mineral that remains stable under weathering conditions, which is in agreement with its preservation in the Tertre Rouge profile and the relative homogeneous composition in REE-elements of the altered schists (TRS-0, 1, 3 samples). Numerous European kaolinite deposits in the Hercynian massif (Fig. 1), developed on granitoids, show a similar accumulation of REE-rich aluminum phosphates that are generally identified as monazite (Dill, 2001; Dill, 2016; Table 1). The Tertre Rouge kaolin deposit differs from these sites in terms of the predominance of florencite; this, specifically, could be related to the unusual nature of the initial parent rock. It is noted that another kaolin deposit is developed on black shales in the Rhenish Massif (Germany), and this also indicates the presence of an uncommon phosphate identified as gorceixite (Dill, 1995).

7.3 Probable hydrothermal origin of Pyrophyllite/Nacrite/Dickite minerals

In addition to the weathering related to pervasive kaolinization, as discussed earlier, the clay mineral assemblages comprising nacrite and dickite—whether associated with pyrophyllite or not—in the mm-thick veins indicate a likely hydrothermal contribution to the Tertre Rouge deposit. All three minerals have been frequently reported in hydrothermal kaolin deposits. More specifically, they have already been referenced in metamorphic black shales within the Central European Hercynian Massif (Ludwig, 1972) or in the Portuguese Iberian Hercynian Massif (Chaminé et al., 2003). Moreover, Choo and Kim (2004) described dickite and quartz, as well certain amounts of nacrite, pyrophyllite, diaspore, alunite, illite, sulfides,

and calcite in a southeastern Korean kaolin deposit formed from volcanic tuff. In Patagonia, pervasive alteration of rhyolitic rocks produced dickite, pyrophyllite, and diaspore (Le Grecco et al., 2012). Chen et al. (2001) identified nacrite and dickite occurrences, sometimes with pyrophyllite, associated with a gold–copper mineralization in North Taiwan. The temperature-cationic activity diagram indicates that pyrophyllite occurs under quartz saturation, at temperatures above 270 °C and a pressure of 100 MPa; in contrast, at temperatures below 270 °C, it is replaced by kaolinite (Inoue, 1995; Sverjensky et al., 1991) (Fig. 13).

For the Tertre Rouge deposit, the detection of nacrite/dickite only within veins, and their close association with pyrophyllite is related to a hydrothermal origin. The main assemblages identified here (pyrophyllite-dickite-nacrite-quartz (TRV-1) and millimetric veins with almost pure nacrite/dickite compositions (TRV-2)) suggest two formation processes for nacrite and dickite. Their euhedral shape in the pyrophyllite-free TRV-2 assemblage suggests direct precipitation from fluids within open veins. The following alteration reaction may have occurred in TRV-1 veins where nacrite/dickite clearly replace pyrophyllite crystals along with a large amount of quartz:

$$Al_2Si_4O_{10}(OH)_2 + H_2O \rightarrow 2SiO_2 + Al_2Si_2O_5(OH)_4$$

Pyrophyllite *Quartz* *nacrite/dickite*

Dickite and nacrite, often described as being associated with pyrophyllite, are considered to be high-temperature polymorphs of kaolinite. The sequence kaolinite → dickite → nacrite has been interpreted from isotopic data as leading to increasing temperatures in hydrothermal deposits in Japan (Marumo, 1989). Kaolinite is progressively replaced by dickite/nacrite with increasing burial depth during diagenesis (e.g. Ruiz Cruz, 2007; Beaufort et al., 1998). However, even though nacrite is commonly associated with high-T alteration/precipitation processes, it appears to remain stable over a large temperature range, which precludes accurate temperature estimates from this mineral alone. Buatier et al. (1996) reported a nacrite

formation temperature of approximately 80–100 °C in the basement of the Lodève Basin (France). Moreover, Buhmann (1988) suggested that nacrite crystallized at ambient temperature on the walls of a tunnel in South Africa. Regarding the Tertre Rouge deposit, two stages of hydrothermal precipitation were recorded by the occurrences of pyrophyllite and nacrite/dickite: the first stage involved high-temperature fluids responsible for the formation of the pyrophyllite (> 270 °C, Inoue (1995)), and the second stage probably involved lower temperatures that led to the replacement of pyrophyllite by quartz and nacrite/dickite (<270 °C, Inoue (1995)).

8. CONCLUSION: A TWO-STAGE KAOLINIZATION EVENT IN THE TERTRE ROUGE DEPOSIT

Based on both textural petrologic and geochemical analyses, the florencite-rich kaolins in the Tertre Rouge deposit are determined to result from a two-stage kaolinization process, as shown below.

The vein-hosted clay assemblages clearly predate the pervasive weathering stage that produced the kaolinite at the expense of the Middle Ordovician schists. This is suggested by kaolinite crystal clusters or micro-veins cutting across the pyrophyllite crystals and the dissolution pits in nacrite/dickite crystals. Based on their occurrence as secant and parallel veins to the cleavage plane S, which is the axial cleavage plane of N110°E trending folds, such veins may be linked to regional-scale ductile dextral simple shearing along the SASZ (Gapais and Le Corre, 1980; Choukroune et al., 1983; Gumiaux et al., 2004; Tartèse et al., 2010, Gapais et al., 2015). Elongated pyrophyllite flakes preserving the same orientation as the cleavage plane S suggest the occurrence of synkinematic hydrothermal precipitation.

There exists considerable evidence of a Late Hercynian hydrothermal event in the immediate vicinity of the Tertre Rouge pit. Centimetric quartz veins occur locally inside the basal schist level, irrespective of the weathering profile, similar to the N150°E thicker quartz veins documented by Lemarchand et al. (2012). These are also Pb-Sb-Au ore deposits (Chauris and Marcoux, 1994; Gloaguen et al., 2007; Pochon et al., 2016, 2017, 2018). In the Bois de la Roche quarry at Saint-Aubin-des-Châteaux, 6 km NW of the Tertre Rouge pit, Gloaguen et al. (2007) identified several hydrothermal stages that precipitated large amounts of pyrite and a variety of sulfarsenides, antimonides, and Sr-Sc phosphates that replaced oolitic ironstone layers within the Lower Ordovician Armorican sandstone formation (see also Möelo et al., 2002, Fig. 2). Hydrothermal fluids started precipitating pyrite/arsenopyrite at about 390–350 °C, and subsequent stages proceeded at lower temperatures of around 300–275 °C. This ore deposition was coeval with the emplacement of the Late Hercynian granites, suggesting a genetic relationship between both events (Late Carboniferous) (Chauris and Marcoux, 1994; Bouchot et al., 2005; Gloaguen et al., 2007). The aforementioned studies also reported the occurrence of dickite. However, the spatial relationship between the Saint-Aubin-des-châteaux ore deposits and the Tertre Rouge kaolins is unclear because of the lack of relevant outcrops between the two sites.

The youngest kaolinization process, which is the most important in terms of a mineable deposit, appears to be controlled primarily by weathering, in agreement with kaolinite-rich weathering profiles documented throughout France (e.g. Bellion, 1979; Boulvais et al., 2000; Estéoule-Choux, 1967, 1983; Thiry et al., 2006; Thomas,1999; Wyns, 1991, 1996; Gaudin et al., 2015). This process overprints a chlorite-muscovite anchizonal-greenschist metamorphism ascribed to Hercynian metamorphism (Ballèvre et al., 2012 and reference therein). More generally, such a development of thick kaolinite weathering profiles is also observed on a

European scale from various Paleozoic metamorphic rocks or granitoids (e.g. Dupuis et al., 1996; Borrelli et al., 2012; Le Pera et al., 2001; Störr, 1975) (Fig. 1).

According to Esteoule-Choux (1983), the important episodes of weathering in Brittany are older than Oligocene; the Upper Cretaceous-Lower Eocene could be a suitable period, but older periods (middle Cretaceous or even Jurassic) cannot be ruled out. Indeed, several in situ “siderolithic” formations on the edges of the French Massif Central (SE of Brittany) and kaolinitic profiles in the Belgian Ardennes (NE of Brittany) indicate especially early Cretaceous ages (e.g. Quesnel et al., 2003; Ruellan et al., 2003; Théveniaut, 2003; Thiry et al., 2004, 2006), by means of paleo-magnetism and/or radiogenic isotopes. These ages are consistent with those proposed by Gaudin et al. (2015) at Penestin (Fig. 2), as deduced from the correlation of the D/H values of kaolins with a time established by Gilg (2000) in Northeast Bavaria.

Acknowledgments

We thank T. Fréva, A. Lessard, J. Boucherie, and V. Cocault for having provided access to the "Tertre rouge" B.N.Z. deposit, as well as assistance during field work. We thank Laurent Lenta from the LPG for preparing the thin sections and Pierre-Emmanuel Petit and Nicolas Stephan from the IMN laboratory (Nantes, France) for their help during the SEM and XRD analyses. We thank H. Dill for his detailed review and relevant suggestions. Financial support was provided by the Centre National de la Recherche Scientifique (CNRS) through its EPOV (Environnements Planétaires et Origines de la Vie) program.

CAPTIONS

Table 1. Occurrences of Kaolinite and associated REE phosphates in the European Hercynian belt.

Table 2. XRD mineralogy of the TRS and TRV samples (bulk sample analyses). Abbreviations of rock-forming minerals (Whitney and Evans, 2010): Qz: Quartz; Mica: Mica; Sme: Smectite; Chl: Chlorite; Kln: kaolinite; Dck: dickite, N: Nacrite, Prl: Pyrophyllite; Flo: Florencite; Rt: Rutile; Gth: Goethite; Hem: Hematite; Jrs: Jarosite. *Identified from glycolated oriented clay fractions, + major mineral, (+) minor mineral.

Table 3. Major element contents of the Tertre Rouge samples (wt%).

Table 4. Trace element contents of the Tertre Rouge samples (ppm).

Table S1. Correlation coefficient matrix for trace elements (correlation coefficients $r^2 > 0.9$ in bold) (P for phosphates; TiO_2 for rutile; K_2O for muscovite/illite).

Figures:

Figure 1. Main rare Earth element-rich kaolinite pits in the European Hercynian massifs with the lithology of their host rock. Labeled pits are listed in Table 1.

Figure 2. a) Schematic map of the Armorican Massif located in the northwestern part of France, in which major crustal-scale shear zones (NASZ: North Armorican Shear Zone and SASZ: South Armorican Shear Zone) and their associated syn-kinematic Carboniferous leucogranites are mapped. The main kaolinite outcrops are plotted according to their protolith lithology (locations after Boulvais et al., 2000; Gaudin et al., 2015). b) Close-up of geological map of the Châteaubriant area simplified from Dadet et al. (1987), Dubreuil et al. (1988), Herrouin et al. (1989) and Trautmann et al. (1987). Neo-Proterozoic: Schist, Lower Ordovician: sandstone (*grès armoricain*) and schist, Middle Ordovician: Schist (Angers-Traveusot formation), Upper Ordovician: Schist, Silurian: Schist, Upper Devonian to Carboniferous: Schist and limestones, Eocene: Kaolin deposit and ferricrete. Mineral and ore-deposits are mapped from Donnot et al., 1973, Méloux et al. (1979), Moëlo et al. (2002) and Gloaguen et al. (2007). c) Map of the Tertre Rouge pit established in April 2016. TRS-#, TRV-# indicate the location of analyzed samples.

Figure 3. Images of the Tertre Rouge pit. TRS-#, TRV-# are locations of analyzed samples. a) Lowermost level of the outcrop composed of greyish schists TRS-0 with a sub-vertical cleavage plane (S). b) Plan view of the pit surface into intermediate level TRS-1 composed of dark grey schist, showing a friable fabric in which the cleavage S is preserved and crosscut both by white and orange veins and quartz veins. People give the scale. c) Upper levels of the outcrop: The dark grey schist starts losing its cohesion (TRS-2) at the bottom, although the cleavage S is still preserved, and it fades (TRS-3) near the top. The bleached unit TRS-3 is crosscut by an irregular erosion surface overlaid by no *in situ* reddish material composed of sandstone embedded in argillaceous matrix. d–i) Clay-rich veins secant or parallel to the cleavage plane S within the friable dark grey TRS-1 unit.

Figure 4. Images of thin sections observed trough optical microscopy of samples: (a) from the lowermost level of the profile (TRS-0, plane polarized light), from the TRV-1d pyrophyllite/kaolin/quartz rich veins within the TRS-1 unit under plane-polarized (b) and cross-polarized light (c), from the bleached TRS-3 unit (d). Prl: pyrophyllite.

Figure 5. Images of thin sections observed through optical microscopy under cross-polarized light of the TRS-0 schist (a, b) and of pyrophyllite/kaolin/quartz-rich veins and vug (d–h). Kln: kaolin (kaolinite, dickite, nacrite), Prl: Pyrophyllite, Qz: Quartz, Fe ox.: Iron oxide.

Figure 6. SEM-EDX images of TRV-1d veins (a, b; BSE mode) and of nacrite/dickite particles from the TRV-2 samples (c-f, SE mode).

Figure 7. Powder XRD patterns of the TRS samples (a, d) and of the TRV samples. Mica: Mica, Kln: kaolinite, N: nacrite, Dck: dickite, Prl: pyrophyllite, Qz: quartz, Flo: Florencite.

Figure 8. Powder XRD patterns of the TRS bulk samples : (a) Normalized in intensity with the mica peak at 9.98 Å to compare the kaolinite abundance between TRS-0 (lowermost unit) and the TRS-1, 2, 3 samples (dark grey and bleached schists), (b) Normalized in intensity with kaolinite to compare the FWHM (< ------ >, crystallinity) between the TRV and the TRS samples.

Figure 9. SEM-EDS maps of P, Ca, Al in the TRS-0c sample.

Figure 10. BSE SEM images and EDS spectrum of florencite particles within the TRS-0c sample. *Chemical formulae of the florencite total oxygen recalculated by stoichiometry from Al, Fe, Ca, Sr, La, Ce, Nd, and P oxides, (1) elements absent from the florencite and likely due to mica and/or kaolinite impurities.

Figure 11. BSE SEM images and EDS spectra of xenotime, monazite, oxidized pyrite, and zircon within the TRS-0c sample.

Figure 12. REE patterns of the TRS and TRV samples.

Figure 13. Temperature logarithmic cation activity ratio diagram in the K_20-Al_2O_3-SiO_2-H_2O system at a total pressure of 100 MPa under quartz saturation (redrafted from Inoue (1995)).

REFERENCES:

Aspandiar, M., Eggleton, R., 2002. Weathering of chlorite: I. Reactions and products in microsystems controlled by the primary mineral. Clays Clay Miner. 50, 685–698.

Ballèvre, M., Bosse, V., Ducassou, C., Pitra, P., 2009. Palaeozoic history of the Armorican Massif: Models for the tectonic evolution of the suture zones. C. R. Geosci. 341, 174-201.

Ballèvre, M., Bosse, V., Dabard, M.P., Ducassou, C., Fourcade, S., Paquette, J.L., Peucat, J.J., Pitra, P., 2012. Histoire géologique du Massif armoricain : actualité de la recherche. Bull. Soc. Géol. Minéral. Bretagne 10-11, 5-96.

Banfield, J.F., Eggleton, R.A, 1989. Apatite replacement and rare earth mobilization, fractionation, and fixation during weathering. Clays Clay Miner. 37, 113-127.

Bayliss, P., Kolitsch, U., Nickel, E. H., Pring, A., 2010. Alunite supergroup: recommended nomenclature. Mineral. Mag., 74, 5, 919-927.

Beaufort, D., Cassagnabère, A., Petit, S., Lanson, B., Berger, G., Lacharpagne, J.C., Johansen, H., 1998. Kaolinite-to-dickite conversion series in sandstone reservoirs. Clay Miner. 33, 297-316.

Bellion, G., 1979. Contribution à l'étude du gisement de kaolin de Ploemeur (Morbihan): caractères, origine. Thesis, Univ. Rennes I, 192 pp.

Berner, Z.A., Puchelt, H., Noeltner, T., Kramar, U., 2013. Pyrite geochemistry in the Toarcian Posidonia Shale of southwest Germany: Evidence for contrasting trace element patterns of diagenetic and syngenetic pyrites. Sedimentol. 60 (2), 548-573.

Berthé, D., Choukroune, P., Jégouzo, P., 1979. Orthogneiss, mylonite and non-coaxial deformation of granites: The example of the South Armorican Shear Zone. J. Struct. Geol. 1, 31-42.

Borrelli, L., Perri, F., Critelli, S., Gullà, G., 2012. Minero-petrographical features of weathering profiles in Calabria, southern Italy. Catena 92, 196-207.

Bouchot V., Ledru P., Lerouge, C., Lescuyer, J. L., Milesi, J.P., 2005. Late Variscan mineralizing systems related to orogenic processes: the French Massif Central. Ore Geol. Rev., 169-197.

Boulvais, P., Vallet, J.M., Estéoule-Choux, J., Fourcade, S., Martineau, F., 2000. Origin of kaolinization in Brittany (NW France) with emphasis on deposits over granites: stable isotope (O, H) constraints. Chem. Geol. 168, 211-223.

Brindley, G.W., Brown, G, 1980. Crystal Structures of Clay Minerals and their X-ray Identification. Brindley, G.W., Brown G (Eds), Mineralogical Society, London, 495 pp.

Brown, M., Dallmeyer, R.D., 1996. Rapid Variscan exhumation and the role of magma in core complex formation: Southern Brittany metamorphic belt, France. J. of Metamorph. Geol. 14, 361-379.

Brumsack, H.J., 2006. The trace metal content of recent organic carbon-rich sediments: implications for Cretaceous black shale formation. Palaeogeogr. Palaeoclimatol. Palaeoecol. 232 (2-4), 344-361.

Buatier, M.D., Potdevin, J.L., Lopez, M., Petit, S., 1996. Occurrence of nacrite in the Lodève Permian basin (France). Eur. J. Mineral. 8, 847-852.

Buhmann, D., 1988. An occurrence of authigenic nacrite. Clays Clay Miner. 36, 137-140.

Burnotte, E., Pirard, E., Michel, G., 1989. Genesis of gray monazites; evidence from the Paleozoic of Belgium. Economic Geology, 84 (5), 1417-1429.

Carron, J.P., Le Guen de Kerneizon, M., Nachit, H., 1994. Variscan granites from Brittany, in: Keppie, J.D. (Ed), Pre-Mesozoic geology in France and related areas. Springer, pp. 231-239.

Chaminé, H.I., Gama Pereira, L.C., Fonseca, P.E., Moço, L.P., Fernandes, J.P., Rocha, F.T., Flores, D., Pinto de Jesus, A., Gomes, C., Soares de Andrade, A.A., Araújo, A., 2003. Tectonostratigraphy of Middle and Upper Palaeozoic black shales from the Porto-Tomar-Ferreira do Alentejo shear zone (W Portugal): new perspectives on the Iberian Massif. Geobios 36, 649-663.

Chang, L.Y., Howie R.A., Zussman, J., 1997. Rock Forming Minerals. Volume 5B: Non-silicates; sulphates, carbonates, phosphates and halides. Harlow, Longman, 392 pp.

Chantraine, J., Autran, A., Cavelier, C., 1996. Carte géologique de la France. BRGM, Orléans.

Chauris, L., 1984. Origine hydrothermale post-magmatique de la kaolinisation à Berrien (Finistère, France). C. R. Acad. Sci. 298, 13-16.

Chauris, L., Marcoux, E., 1994. Metallogeny of Armorican Massif, in: Keppie, J.D. (Ed), Pre-Mesozoic geology in France and related area. Springer, Berlin Heidelberg New York, pp 243-264.

Chauris, 1996. Vue d’ensemble sur les occurrences de kaolin d'origine hydrothermale en Bretagne (France). Bull. Soc. Sci. Nat. Ouest France, 18(4), 157-188.

Chauvel, J.J., Phan, K.D., 1965. Présence d’apatite strontianifère dans le minerai de fer de l’Ordovicien inférieur de Bretagne. C. R. Acad. Sci. Paris 260, 2855-2857.

Chauvel, J.J., 1974. Les minerais de fer de l’Ordovicien inférieur du bassin de Bretagne-Anjou, France. Sedimentol. 21, 127-147.

Chen, Y.C., Wang, M.K., Yang, D.S., 2001. Mineralogy of dickite and nacrite from northern Taiwan. Clays and Clay Minerals, 49, 586–595.

Choo, C.O., Kim, S.J., 2004. Dickite and other kaolin polymorphs from an Al-rich kaolin deposit formed in volcanic tuff, southeastern Korea. Clays Clay Miner., 52 (6), 749-759.

Choukroune, P., Lopez-Munoz, M., Ouali, J., 1983. Cisaillement ductile sud-armoricain et déformations discontinues associées : mise en évidence de la déformation régionale non coaxiale dextre. C. R. Acad. Sci. Paris, 296, 657-660.

Churchman, G.J., 1978. Studies on a climax sequence in soils in tussock grasslands. Mineral. N. Z. J. Sci. 21, 467-480.

Churchman, G.J., 1980. Clay minerals formed from micas and chlorites in some New Zealand soils. Clay Miner. 15, 59-76.

Clauer, N., Fallick, A.E., Galán, E., Aparicio, P., Miras, A., Fernández-Caliani, J.C., Aubert, A., 2015. Stable isotope constraints on the origin of kaolin deposits from Variscan granitoids of Galicia (NW Spain). Chem. Geol. 417, 90-101.

Coveney, R., Pasava, J., 2004. Diverse connections between ores and organic matter. Ore Geol. Rev. 24, 1-5.

Cuney, M., Marignac, C., Weisbrod, A., 1992. The Beauvoir topaz-lepidolite albite granite (Massif Central, France): the disseminated magmatic Sn-Li-Ta-Nb-Be mineralization. Econ. Geol. 87, 1766–1794.

Dabard, M.P., Loi, A., Paris, F., 2007. Relationship between phosphogenesis and sequence architecture: Sequence stratigraphy and biostratigraphy in the Middle Ordovician of the Armorican Massif (NW France). Palaeogeogr. Palaeoclimatol. Palaeoecol. 248, 309-356.

Dadet, P., Herrouin, Y., Laville, P., Paris, F., 1987. Carte géologique de la France (1/50 000) – Bain-de-Bretagne (388). BRGM, Orléans.

Dehaine, Q., Filippov, L.O., 2015. Rare earth (La, Ce, Nd) and rare metals (Sn, Nb, W) as by-product of kaolin production, Cornwall: Part1: Selection and characterization of the valuable stream. Min. Eng. 76, 141-153.

Dehain, Q., Filippov, L.O., Glass, H.J., Rollinson, G., 2019. Rare-metal granites as a potential source of critical metals: A geometallurgical case study. Ore Geol. Rev. 104, 384-402.

Devismes, P., Guigues, J., Laurent, Yvette, L., Parfenoff, A., 1968. Première découverte de florencite en France. Bull. Soc. Fr. Minéral. Cristallogr. 91(5), 500-502.

Dill, H.G., Fricke, A., Henning, K.-H., 1995. The origin of Ba- and REE-bearing aluminium-phosphate-sulphate minerals from the Lohrheim kaolinitic clay deposit (Rheinisches Schiefergebirge, Germany). Applied Clay Sci. 10, 231-245.

Dill, H.G., Bosse, H.R., Henning, K.H., Fricke, A., Ahrend, H., 1997. Mineralogical and chemical variations in hypogene and supergene kaolin deposits in a mobile fold belt - The Central Andes of northwestern Peru. Mineral. Deposit, 32, 149-163.

Dill, H.G., 2001. The geology of Aluminium Phosphates and sulfates of the alunite supergoup. Earth-Sci. Rev. 53, 35– 93.

Dill, H.G., 2010. The “chessboard” classification scheme of mineral deposits: Mineralogy and geology from aluminum to zirconium. Earth-Sci. Rev. 100, 1-420.

Dill, H.G., 2016. Kaolin: Soil, rock and ore: From the mineral to the magmatic, sedimentary and metamorphic environments. Earth-Sci. Rev. 161, 16-129.

Dill, H.G., 2017. Residual clay deposits on basement rocks: The impact of climate and the geological setting on supergene argillitization in the Bohemian Massif (Central Europe) and across the globe. Earth-Sci. Rev. 165, 1-58.

Donnot, M., Guigues, J., Lulzac, Y., Magnien, A., Parfenoff, A., Picot, P., 1973. Un nouveau type de gisement d’europium: la monazite grise à europium en nodules dans les schistes paléozoïques de Bretagne. Miner. Deposita 8, 7-18.

Dubreuil, M., Blaise, J., Cavet, P., Diot, H., Gruet, M., 1988. Carte géologique de la France (1/50 000) – Saint-Mars-la-Jaille (421). BRGM, Orléans.

Dudoignon, P., Beaufort, D., Meunier, A., 1988. Hydrothermal and supergene alterations in the granitic cupola of Montebras, Creuse, France. Clays Clay Miner. 36, 505-520.

Dupuis, C., Charlet, J.M., Dejonghe, Thorez, J., 1996. Reconnaissance par carottage des paleoalterations kaolinisées mésozoïque de la Haute Ardenne (Belgique). Le sondage de Transinne (194E−495): premiers résultats. Ann. Soc. Géol. Belg. 2, 91-109.

Durand, J., Noblet, C., 1986. Paléocourants dans la Formation du Grès armoricain: persistance des mécanismes de transport en domaine cratonique. Rev. Géol. Dyn. Géogr. Phys. 27, 13-26.

Estéoule-Choux, J., 1967. Contribution à l'étude des argiles du massif armoricain. Thesis, Univ. Rennes I, 319 pp.

Estéoule-Choux, J., 1983. Altérations et silicifications au Tertiaire dans le Massif Armoricain. Géol. Fr. 4, 345-352.

Faure, M., Bé Mézème, E., Cocherie, A., Rossi, P., Chemenda, A., Boutelier, D., 2008. Devonian geodynamic evolution of the Variscan Belt, insights from the French Massif central and Massif Armoricain, Tectonics. Tectonic, 27, TC2005 doi:10.1029/2007TC002115.

Fernández-Caliani, J.C., Galán. E., P. A., Apapricio, P., Miras, A., Marquez, M.G., 2010. Origin and geochemical evolution of the Nuevo Montecastelo kaolin deposit (Galicia, NW Spain). Applied Clay Sci. 49, 91-97.

Gaboreau, S., Beaufort, D., Vieillard, P., Patrier, P., Bruneton, P., 2005. Aluminum phosphate-sulfate minerals associated with Proterozoic unconformity-type uranium deposits in the East Alligator River Uranium Field, Northern Territories, Australia. Can. Mineral. 43(2), 813-827.

Galán, E., Aparicio, P., Fernández-Caliani, J.C., Miras, A., Márquez, M.G., Fallick, A.E., Clauer, N., 2016. New insights on mineralogy and genesis of kaolin deposits: The Burela kaolin deposit (Northwestern Spain). Appl. Clay Sci. 131, 14-26.

Galán, E., Fernández-Caliani, J.C., Miras, A., Aparicio, P., Márquez, M.G., 2007. Residence and fractionation of rare earth elements during kaolinization of alkaline peraluminous granites in NW Spain. Clay Min. 42, 341–352.Gapais, D., Brun, J.P., Gumiaux, C., Cagnard, F., Ruffet, G., Le Carlier de Veslud, C., 2015. Extensional tectonics in the Hercynian Armorican belt (France). An overview. Bulletin de la Société Géologique de France 186, 117–129.

Gapais, D, Brun, J.P., Gumiaux, C., Cagnard, F., Ruffet, G., Le Carlier De Veslud, C., 2015. Extensional tectonics in the Hercynian Armorican belt (France). An overview. Bull. Soc. Geol. Fr 186(2-3), 117-129.

Gapais, D., Le Corre, C., 1980. Is the Hercynian belt of Brittany a major shear zone? Nature 288, 574-576.

Gaudin, A., Ansan, V., Rigaudier, T., 2015. Mineralogical and $\delta^{18}O$-δD isotopic study of kaolinized micaschists at Penestin, Armorican Massif, France: New constraint in the kaolinization process. Catena 133, 97-106.

Gilg, H.A., 2000. D–H evidence for the timing of kaolinization in Northeast Bavaria, Germany. Chem. Geol. 170, 5-18.

Gloaguen, E., Branquet, Y., Boulvais, P., Moëlo, Y., Chauvel, J.J., Chiappero, P.J., Marcoux, E., 2007. Palaeozoic oolitic ironstone of the French Armorican Massif: a chemical and structural trap for orogenic base metal-As-Sb-Au mineralisation during Hercynian strike-slip deformation. Miner. Deposita 42, 399-422.

Grecco, L.E., Marfil, S.A., Maiza, P.J., 2012. Mineralogy and geochemistry of hydrothermal kaolins from the Adelita mine, Patagonia (Argentina); relation to other mineralization in the area. Clay Miner. 47, 131-146.

Guillocheau, F., Rolet, M., 1982. La sédimentation paléozoïque ouest-Armoricaine. Bull. Soc. Géol. Minéral. Bretagne 14, 45-62.

Gumiaux, C., Gapais, D., Brun, J.P., Chantraine, J., Ruffet, G., 2004. Tectonic history of the Hercynian armorican Shear belt (Brittany, France). Geodyn. Acta 17, 289-307.

Herrouin, Y., Dadet, P., Guigues, J., Laville, P., Talbo, H., 1989. Carte Géologique de la France (1/50 000) - Châteaubriant (389). BRGM, Orléans.

Höhn, S, Frimmel, H.E., Pasava, J., 2014. The rare earth element potential of kaolin deposits in the Bohemian Massif (Czech Republic, Austria). Miner Deposita 49, 967-986.

Holland, H.D., 1979. Metals in black shales; a reassessment. Econ. Geol. 74 (7), 1676-1680.

Inoue, A., 1995. Formation of clay minerals in hydrothermal environments, in: Velde B. (Ed), Origin and Mineralogy of Clays. Springer, Berlin Heidelberg, New York, pp. 268-329.

Janeycky, J., Ewing, R.C., 1996. Florencite-(La) with fissiogenic REEs from a natural fission reactor at Bangombe, Gabon. Am. Mineral. 81, 1263-1269.

Jégouzo, P., 1980. The south Armorican Shear Zone. J. Struct. Geol. 2, 39-47.

Johnson, S.C., Large, R.R., Coveney, R.M., Kelley, K.D., Slack, J.F., Steadman, J.A., Gregory, D.D., Sack, P.J., Meffre, S., 2017. Secular distribution of Highly Metalliferous Black Shales corresponds with Peaks in Past Atmosphere Oxygenation. Mineralium Deposita 52, 791-798.

Kalinowski, B.E., Schweda, P., 1996. Kinetics of muscovite, phlogopite, and biotite dissolution and alteration at pH 1-4, room temperature. Geochim. Cosmochim. Acta 60(3), 367-385.

Kuzvart, M. 1992. Kaolin deposits of Central Europe. Clay Sci. 8, 319-327.

Lanson, B., Velde, B., Meunier, A., 1998. Late-stage diagenesis of illitic clay minerals as seen by decomposition of X-ray diffraction patterns: contrasted behaviors of sedimentary basins with different burial histories. Clays Clay Miner. 46, 69-78.

Large, R.R., Maslennikov, V.V., Robert, F., 2007. Multistage Sedimentary and Metamorphic Origin of Pyrite and Gold in the Giant Sukhoi Log Deposit, Lena Gold Province, Russia. Econ. Geol. 102, 1233-1267.

Le Corre, C., Auvray. B., Ballèvre, M., Robardet, M., 1991. Le Massif Armoricain. Sci. Geol. Bull, 44, 31-103.

Lemarchand, J., Boulvais, P., Gaboriau, M., Boiron, M.C, Tartèse, R., Cokkinos, M., Bonnet, S., Jégouzo, P., 2012. Giant quartz vein formation and high-elevation meteoric fluid infiltration into the South Armorican Shear Zone: geological, fluid inclusion and stable isotope evidence. J. Geol. Soc. London 169, 17-27.

Le Pera, E., Critelli, S., Sorriso-Valvo, M., 2001. Weathering of gneiss in Calabria, Southern Italy. Catena 42, 1-15.

Linnen, R.L., Samson, I.M., Williams-Jones, A.E., Chakhmouradian, A.R., 2014. 13.21 - Geochemistry of the Rare-Earth Element, Nb, Ta, Hf, and Zr Deposits, in: Holland, H.D., Turekian, K.K. (Eds), Treatise on Geochemistry. Second ed. Elsevier, pp. 543-568.

Ludwig, V., 1972. Die Paragenese Muscovit, Pyrophyllit, 7 Å - Chlorit und Kaolinit imSilur des Frankenwaldes (NE-Bayern). Neues Jahrbuch Geologie Paläontologie Monatshefte, 303-305.

Marumo, K., 1989. Genesis of kaolin minerals and pyrophyllite in Kuroko deposits of Japan: implications for the origins of the hydrothermal fluids from mineralogical and stable isotope data. Geochim. Cosmochim. Ac. 53, 2915-2924.

Méloux, J., Rouveyrol, P., Guigues, J., Dumas, J., Durand, G., Gorichon, A., Le Fur, Y., Lemarchand, R., Mulot, B., 1979. Carte des gîtes minéraux de la France - Nantes. BRGM, Orléans.

Millot, G., 1964. Geologie des Argiles. Masson Eds., Paris.

Moëlo, Y., Lulzac, Y., Rouer, O., Palvadeau, P., Gloaguen, E., Léone, P., 2002. Scandium mineralogy: pretulite with scandian zircon and xenotime-(Y) within an apatite-rich oolitic ironstone from Saint-Aubin-des-Châteaux, Armorican Massif, France Can. Mineral. 40, 1657-1673.

Nagy, G., Draganits, E., Demény, A., Panto, G., Arkai, P., 2002. Genesis and transformations of monazite, florencite and rhabdophane during medium grade metamorphism: examples from the Sopron Hills, Eastern Alps. Chem. Geol. 191(1-3), 25-46.

Nicolas, J., 1956. Contribution à l'étude géologique et minéralogique de quelques gisements de kaolins bretons. Thesis, Univ. Paris, 254 pp.

Nriagu, J.O., Moore P.H., 1984. Phosphate Minerals. Ed. Springer Berlin, New York, Tokyo.

Pochon, A., Gapais, D., Gloaguen, E., Gumiaux, C., Branquet, Y., Cagnard, F., Martelet, G., 2016. Antimony deposits in the Variscan Armorican belt, a link with mafic intrusives? Terra Nova 28 (2), 138-145.

Pochon, A., Beaudoin, G., Branquet, Y., Boulvais, P., Gloaguen, E., Gapais, D., 2017. Metal mobility during hydrothermal breakdown of Fe-Ti oxides: Insights from Sb-Au mineralizing event (Variscan Armorican Massif, France). Ore Geol. Rev. 91, 66-99.

Pochon, A., Gloaguen, E., Branquet, Y., Poujol, M., Ruffet, G., Boiron, M.C., 2018. Variscan Sb-Au mineralization in Central Brittany (France): A new metallogenic model derived from the Le Semnon district. Ore Geol. Reviews 97, 109-142.

Pouliot, G., Hoffmann, H.J., 1981. Florencite: A first occurrence in Canada. Can. Mineral. 19, 535-540.

Quesnel, F., Thiry, M., Simon-Coinçon, R., Théveniaut, H., Wyns, R., 2003. Paléopaysages sidérolithiques au nord du Massif Central. 9ème Congrès Français de Sédimentologie, Bordeaux, 14 au 16 oct., Livre des résumésPubl. ASF, Paris 38 pp. 416-417.

Raimbault, L., Cuney, M., Azencott, C., Duthou, J.-L., Joron, J.-L., 1995. Geochemical Evidence for a Multistage Magmatic Genesis of Ta-Sn-Li Mineralization in the Granite at Beauvoir, French Massif Central. Econ. Geol. 90, 548-576.

Rasmussen, B., 1996. Early-diagenetic REE phosphate minerals (Florencite, Gorceixite, Crandallite and Xenotime) in marine sandstones: a major sink for oceanic phophorus. Amer. J. Sci., 296, 605-632.

Repina, S.A. Popova, V.I. Churin, E.I., Belogub, E.V., Khille, V.V., 2011. Florencite (Sm) - (Sm, Nd)$Al_3(PO_4)_2(OH)_6$: A New Mineral Species of the Alunite - Jarosite Group from the Subpolar Urals1 S. A. Geol. Ore Deposits, 53 (7), 564-574.

Rudnick, R.L., Gao, S., 2014. Composition of the Continental Crust, in: Rudnick, R.L., Holland, H.D., Turekian, K.K. (Eds.), Treatise on Geochemistry, The Crust (vol. 4). Elsevier-Pergamon, Oxford 2nd edition, pp. 1-45.

Ruellan, P.-Y., Moreau, M.-G., Simon-Coinçon, R., Thiry, M., 2003. Formations “sidérolithiques” du Lembron (Massif central): paléoaltérations, paléoreliefs et datation. 9ème Congrès Français de Sédimentologie, Bordeaux, 14 au 16 oct., Livre des résumés Publ. ASF, Paris 38 pp. 446-447.

Ruiz Cruz, M.D., 2007. Genesis and evolution of the kaolin-group minerals during the diagenesis and the beginning of metamorphism, in: Nieto, F., Jiménez-Millán, J. (Eds), Diagenesis and Low-temperature Metamorphism. Theory, Methods and Regional Aspects. Seminarios SEM. 3, 41-52.

Samalens, N., Barnes, S.J., Sawyer, E.W., 2017. The role of black shales as a source of sulfur and semimetals in magmatic nickel-copper deposits: Example from the Partridge River Intrusion, Duluth Complex, Minnesota, USA. Ore Geol. Rev. 81, 173-187.

Schwab, R.G., Herold, H., Da Costa, M.L., De Oliveira, N.P., 1989. The formation of aluminous phosphates through lateritic weathering of rocks, in Zographou, S.A. (Ed), Weathering: Its products and deposits, vol. II: Products deposits – geotechnics. Theophrastus, Athens, pp 369-386.

Störr, M., 1975. Kaolin Deposits of the GDR in the Northern Region of the Bohemian Massif. Ernst-Moritz-Arndt-Universitaet, Greifswald, 243 pp.

Sverjensky, D.A., Hemley J.J., D’angelo, W. M., 1991. Thermodynamic assessment of hydrothermal alkali feldspar-mica- aluminosilicate equilibria. Geochim. Cosmochim. Acta 55, 989- 1004.

Tartèse, R., Boulvais, P., Poujol, M., Chevalier, T., Paquette, J.L., Ireland, T.R., Deloule, E., 2012. Mylonites of the South Armorican Shear Zone: Insights for crustal-scale fluid flow and water-rock interaction processes. J. Geodyn. 56-57, 86-107.

Théveniaut, H., 2003. Paleomagnetism as an indirect dating tool of lateritic weathering profiles (saprolite, bauxite and ferricrete): theoretical bases, method, results in French Guiana, Africa and Europe, in: Paleoweathering and paleosurfaces in the Ardennes-Eifel region –Preizerdaul, Luxembourg, Géol. Fr., 1, 89-90.

Taylor, S.R., McLennan, S.H., 1985. The continental crust; its composition and evolution. Blackwell, Oxford, 312 pp.

Thiry, M., Moreau, M. G., Simon-Coinçon, R., Ruellan, P.Y., 2004. Datation des paléoaltérations et des événements géodynamiques continentaux – II – paléoaltérations, paléoreliefs et datation des formations “sidérolithiques” du Lembron. Rapport Armines/Ecole des Mines, LHM/RD/2004/03, 76 pp.

Thiry, M., Quesnel, F., Yans, J., Wyns, R., Vergari, A., Théveniaut, H., Simon-Coinçon, R., Ricordel, C., Moreau, M.G., Giot, D., Dupuis, C., Bruxelles, L., Barbarand, J., Baele, J.M., 2006. Continental France and Belgium during the early Cretaceous: paleoweatherings and paleolandforms. Bull. Soc. Geol. Fr. 177, 155–175.

Thomas, E., 1999. Evolution cénozoïque d'un domaine de socle: le Massif armoricain. Apport de la cartographie des formations superficielles Géosciences RennesUniv. Thesis, Univ. Rennes 1, 126 pp.

Trautmann, F., Donnot, M., Lemaire, D., Cagnet-Mawhin, M.P., 1987. Carte géologique de la France (1/50 000) - Nozay (420). Brgm, Orléans.

Tribovillard, N., Algeo, T.J., Lyons, T., Riboulleau, A., 2006. Trace metals as paleoredox and paleoproductivity proxies: an update. Chem. Geol. 232 (1-2), 12-32.

Vigneresse, J. L., Brun, J. P., 1983. Les leucogranites armoricains. Structures et mise en place des granites hercyniens. Bull. Soc. Géol. Fr. 25 (3), 357–366.

Ward, C.R., Corcoran, J.F., Saxby, J.D., Read, H.W., 1996. Occurrence of phosphorus minerals in Australian coal seams. Int. J. Coal Geol. 30 (3), 185-210.

Wedepohl, K., 1971. Environmental influences on the chemical composition of shales and clays. Phys. Chem. Earth 8, 305-333.

Whitney, D.L. Evans, B.W, 2010. Abbreviations for names of rock-forming minerals. Am. Min. 95, 185-187.

Wilson, I.R., Jiranek, J., 1995. Kaolin deposits of the Czech Republic and some comparisons with south-west England. Proceedings of the Ussher Societ, 8, 357-362.

Wilson, M.J., Bain, D.C., Duthie, D.M.L., 1984. The soil clays of Great Britain. II. Scotland. Clay Miner. 19, 709-735.

Wilson, M.J., 1999. The origin and formation of clay minerals in soils: past, present and future perspectives. Clay Miner. 34, 7-25.

Wyns, R., 1991. Evolution tectonique du bâti armoricain oriental au Cénozoïque d'après l'analyse des paléosurfaces continentales et des formations géologiques associées. Géol. Fr. 3, 11-42.

Wyns, R., 1996. Essai de quantification de la composante verticale de la déformation finie au Cénozoïque en Poitou, Limousin occidental et dans la plate-forme nord-aquitaine d'après l'analyse des paléosurfaces continentales et des sédiments associés. Rapport BRGM No. 2238, 83 pp.

Zou, J., Tian H and Li T., 2016. Geochemistry and Mineralogy of Tuff in Zhongliangshan Mine, Chongqing, Southwestern China. Minerals, 6 (47), 1-20.

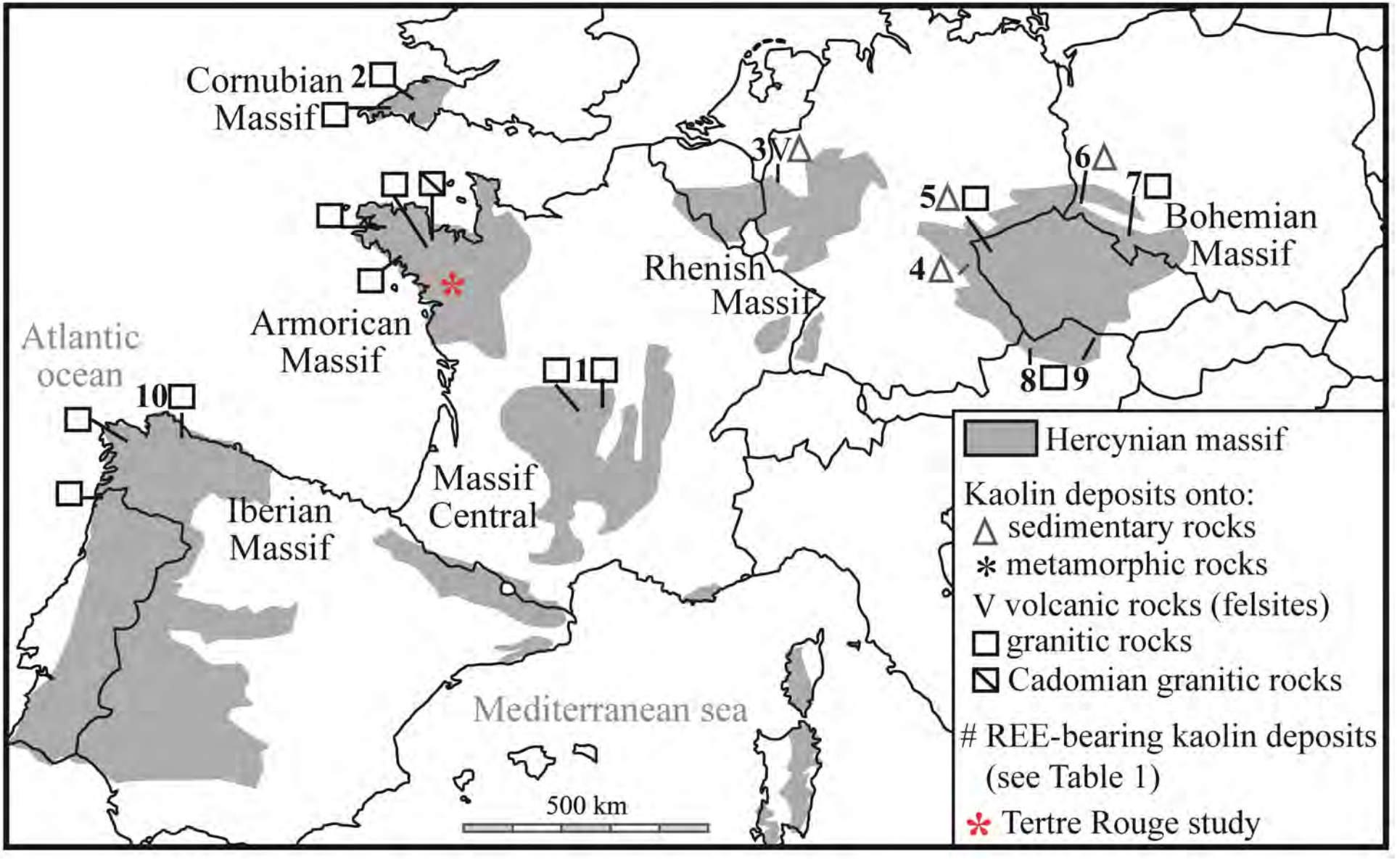
Cornubian Massif
2
Armorican Massif
Atlantic ocean
10
Iberian Massif
Massif Central
1
Rhenish Massif
3
V
5
4
6
7
Bohemian Massif
8
9
Mediterranean sea
500 km
Hercynian massif
Kaolin deposits onto:
sedimentary rocks
metamorphic rocks
V volcanic rocks (felsites)
granitic rocks
Cadomian granitic rocks
REE-bearing kaolin deposits (see Table 1)
Tertre Rouge study

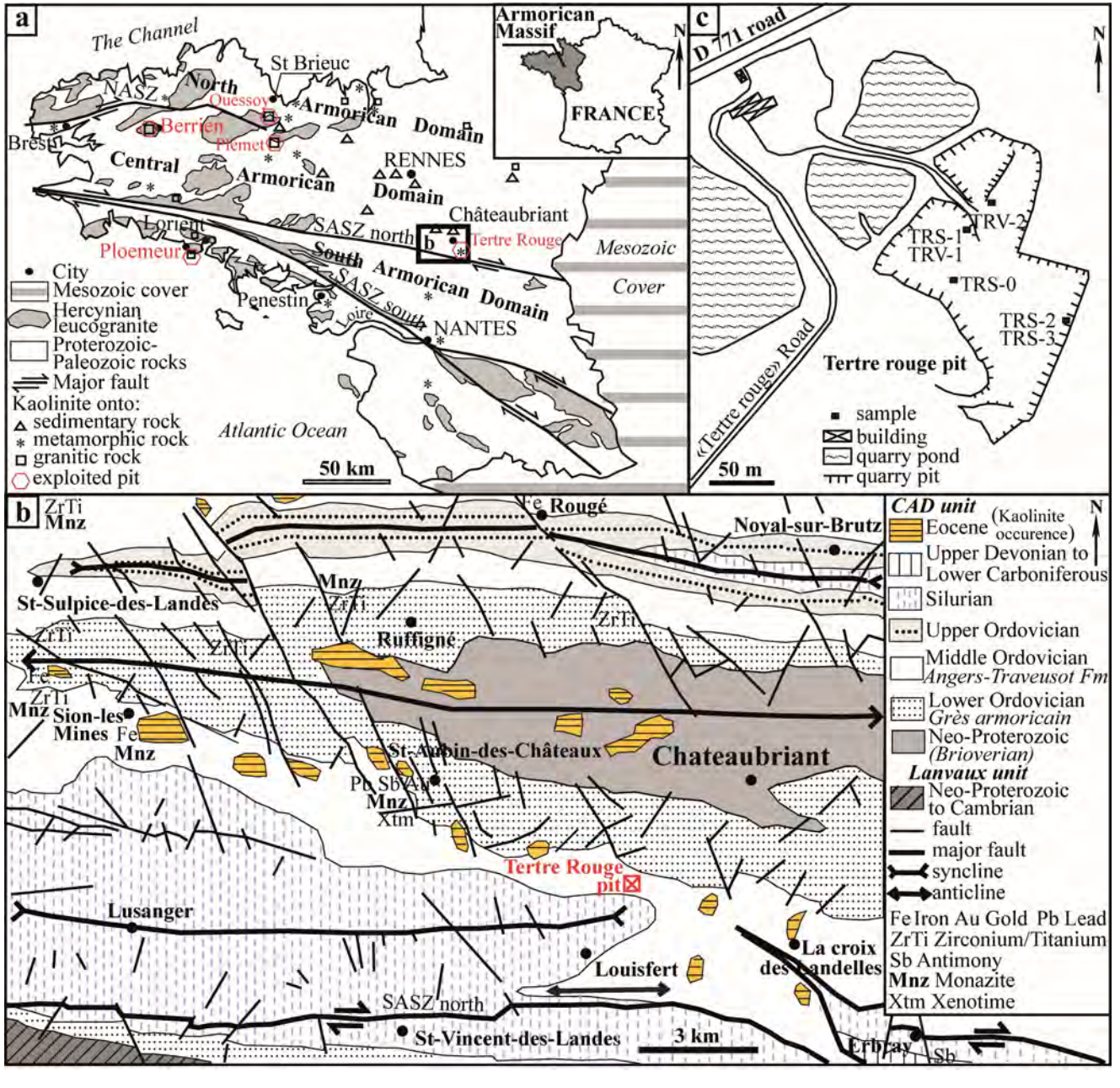
a
The Channel
St Brieuc
North
NASZ
Quessoy
Armorican
Domain
Berrien
Plémet
Brest
Central
Armorican
Domain
RENNES
Châteaubriant
Lorient
SASZ north
b
Tertre Rouge
Ploemeur
South
Armorican Domain
SASZ south
Penestin
Loire
NANTES
Mesozoic
Cover
City
Mesozoic cover
Hercynian leucogranite
Proterozoic-Paleozoic rocks
Major fault
Kaolinite onto:
sedimentary rock
metamorphic rock
granitic rock
exploited pit
Atlantic Ocean
50 km
Armorican Massif
FRANCE
N
c
D 771 road
N
TRV-2
TRS-1
TRV-1
TRS-0
TRS-2
TRS-3
Tertre rouge pit
«Tertre rouge» Road
sample
building
quarry pond
quarry pit
50 m
b
ZrTi
Mnz
Fe
Rougé
Noyal-sur-Brutz
St-Sulpice-des-Landes
Mnz
ZrTi
Ruffigné
ZrTi
ZrTi
ZrTi
Fe
ZrTi
Mnz
Sion-les-Mines
Fe
Mnz
St-Aubin-des-Châteaux
Chateaubriant
Pb Sb Au
Mnz
Xtm
Tertre Rouge pit
Lusanger
Louisfert
La croix des Landelles
SASZ north
St-Vincent-des-Landes
3 km
Erbray
Sb
CAD unit
Eocene (Kaolinite occurence)
Upper Devonian to Lower Carboniferous
Silurian
Upper Ordovician
Middle Ordovician
Angers-Traveusot Fm
Lower Ordovician
Grès armoricain
Neo-Proterozoic
(Brioverian)
Lanvaux unit
Neo-Proterozoic to Cambrian
fault
major fault
syncline
anticline
Fe Iron Au Gold Pb Lead
ZrTi Zirconium/Titanium
Sb Antimony
Mnz Monazite
Xtm Xenotime
N

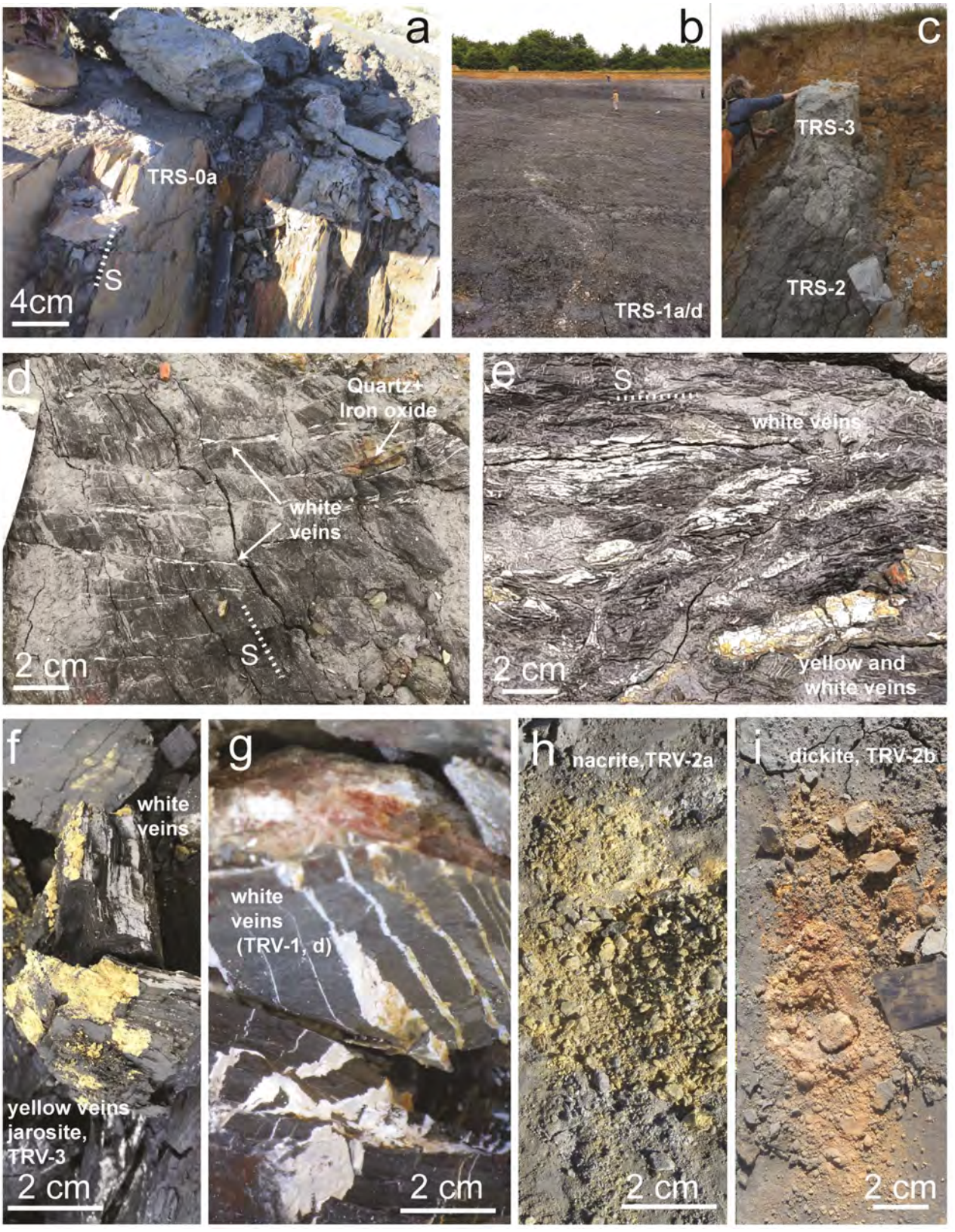
a
TRS-0a
S
4cm
b
TRS-1a/d
c
TRS-3
TRS-2
d
Quartz+
Iron oxide
white
veins
S
2 cm
e
S
white veins
2 cm
yellow and
white veins
f
white
veins
yellow veins
jarosite,
TRV-3
2 cm
g
white
veins
(TRV-1, d)
2 cm
h
nacrite,TRV-2a
2 cm
i
dickite, TRV-2b
2 cm

carbonaceous
matter
d
0.5 mm

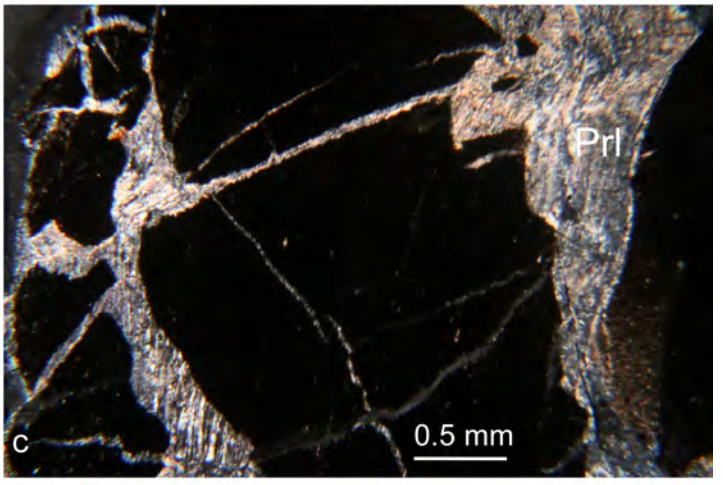
Prl
c
0.5 mm

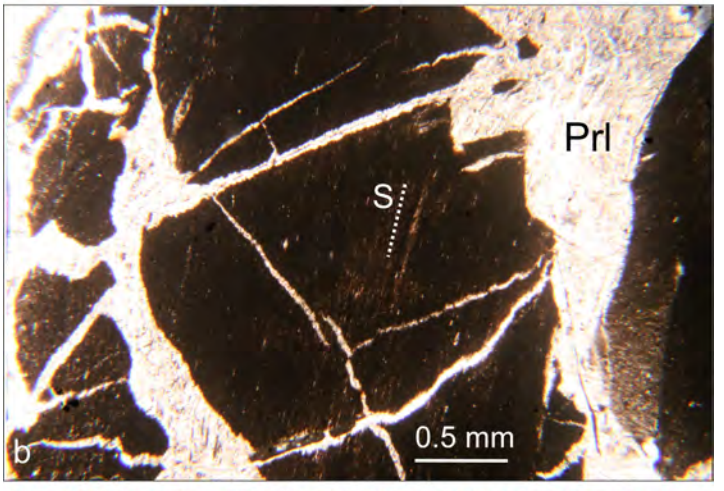
Prl
S
b
0.5 mm

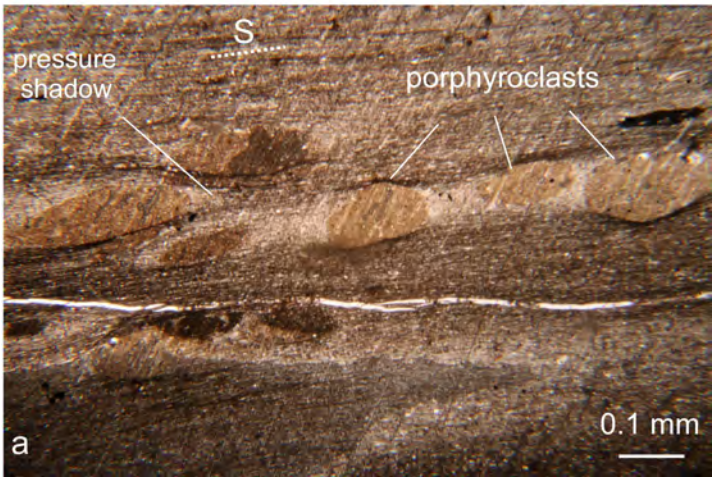
S
pressure
shadow
porphyroclasts
a
0.1 mm

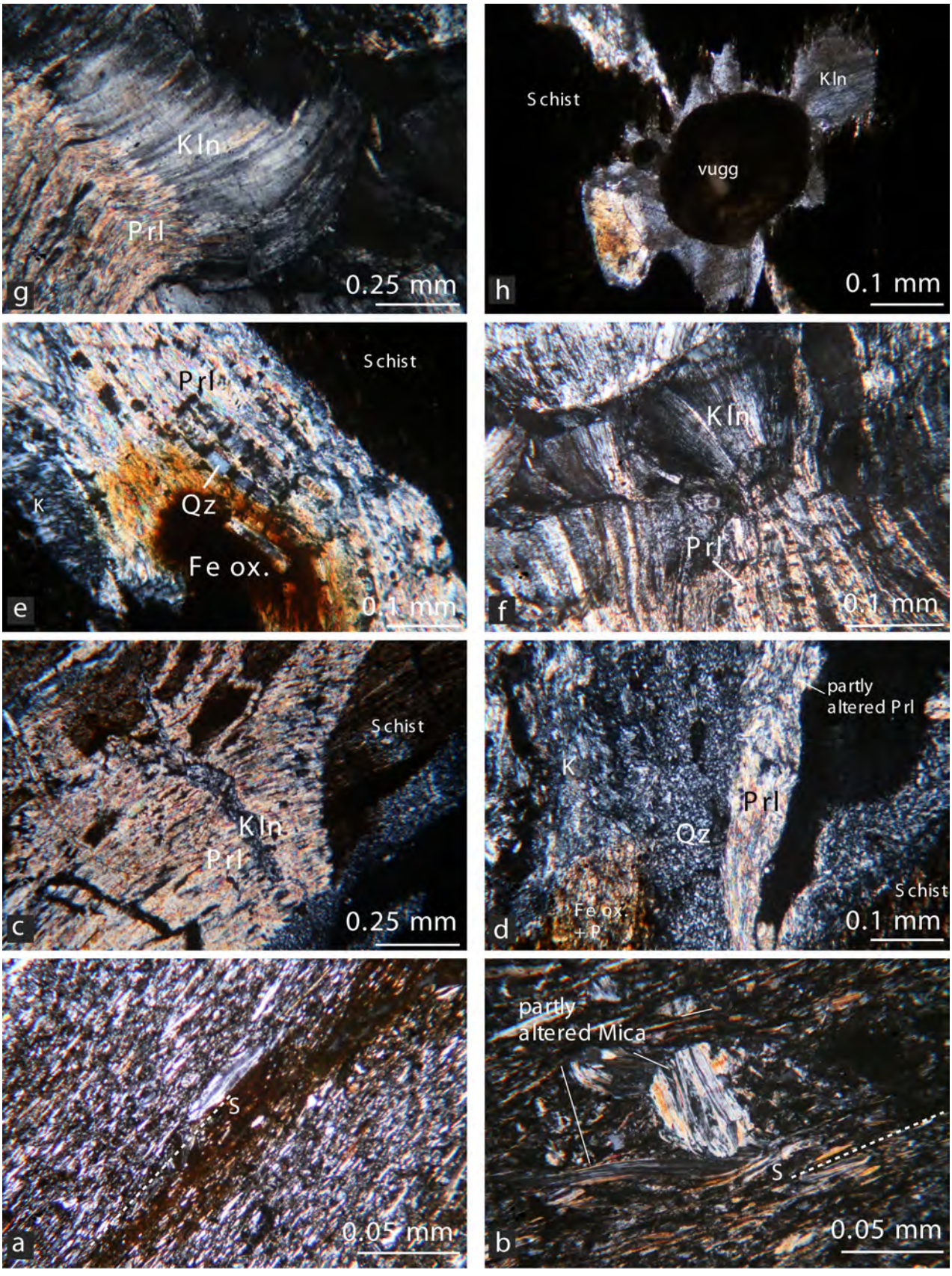
Kln
Prl
0.25 mm
g
Schist
Kln
vugg
0.1 mm
h
Prl
Schist
K
Qz
Fe ox.
0.1 mm
e
Kln
Prl
0.1 mm
f
Schist
Kln
Prl
0.25 mm
c
partly
altered Prl
K
Prl
Qz
Schist
Fe ox.
+ P
0.1 mm
d
S
0.05 mm
a
partly
altered Mica
S
0.05 mm
b

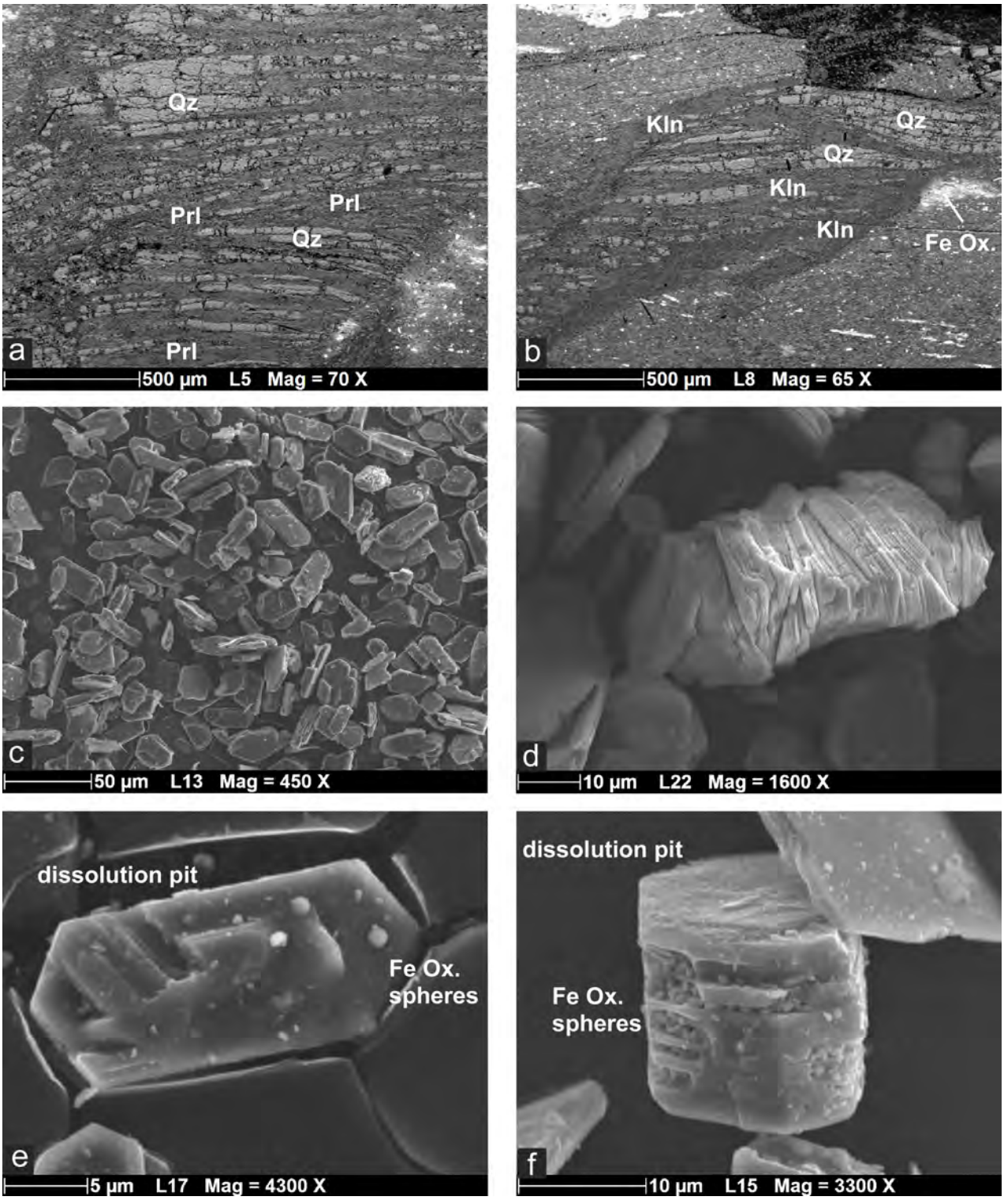
Qz
Prl
Prl
Qz
Prl
a
500 µm L5 Mag = 70 X
Kln
Qz
Qz
Kln
Kln
Fe Ox.
b
500 µm L8 Mag = 65 X
c
50 µm L13 Mag = 450 X
d
10 µm L22 Mag = 1600 X
dissolution pit
Fe Ox.
spheres
e
5 µm L17 Mag = 4300 X
dissolution pit
Fe Ox.
spheres
f
10 µm L15 Mag = 3300 X

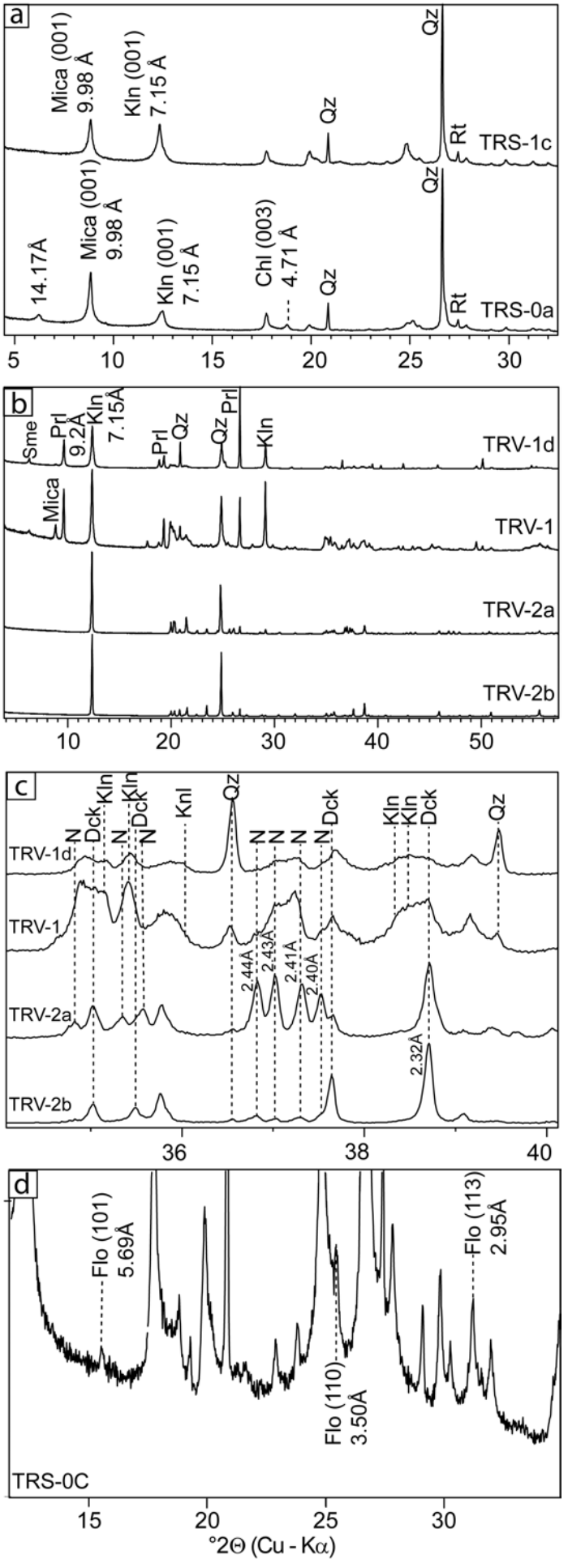
a
Mica (001)
9.98 Å
Kln (001)
7.15 Å
Qz
Qz
Rt
TRS-1c
14.17Å
Mica (001)
9.98 Å
Kln (001)
7.15 Å
Chl (003)
4.71 Å
Qz
Qz
Rt
TRS-0a
5
10
15
20
25
30
b
Sme
Prl
9.2Å
Kln
7.15Å
Prl
Qz
Qz
Prl
Kln
TRV-1d
Mica
TRV-1
TRV-2a
TRV-2b
10
20
30
40
50
c
N
Dck
Kln
N
Kln
N
Dck
Knl
Qz
N
N
N
N
Dck
Kln
Kln
Dck
Qz
TRV-1d
TRV-1
2.44Å
2.43Å
2.41Å
2.40Å
TRV-2a
2.32Å
TRV-2b
36
38
40
d
Flo (101)
5.69Å
Flo (110)
3.50Å
Flo (113)
2.95Å
TRS-0C
15
20
25
30
°2Θ (Cu - Kα)

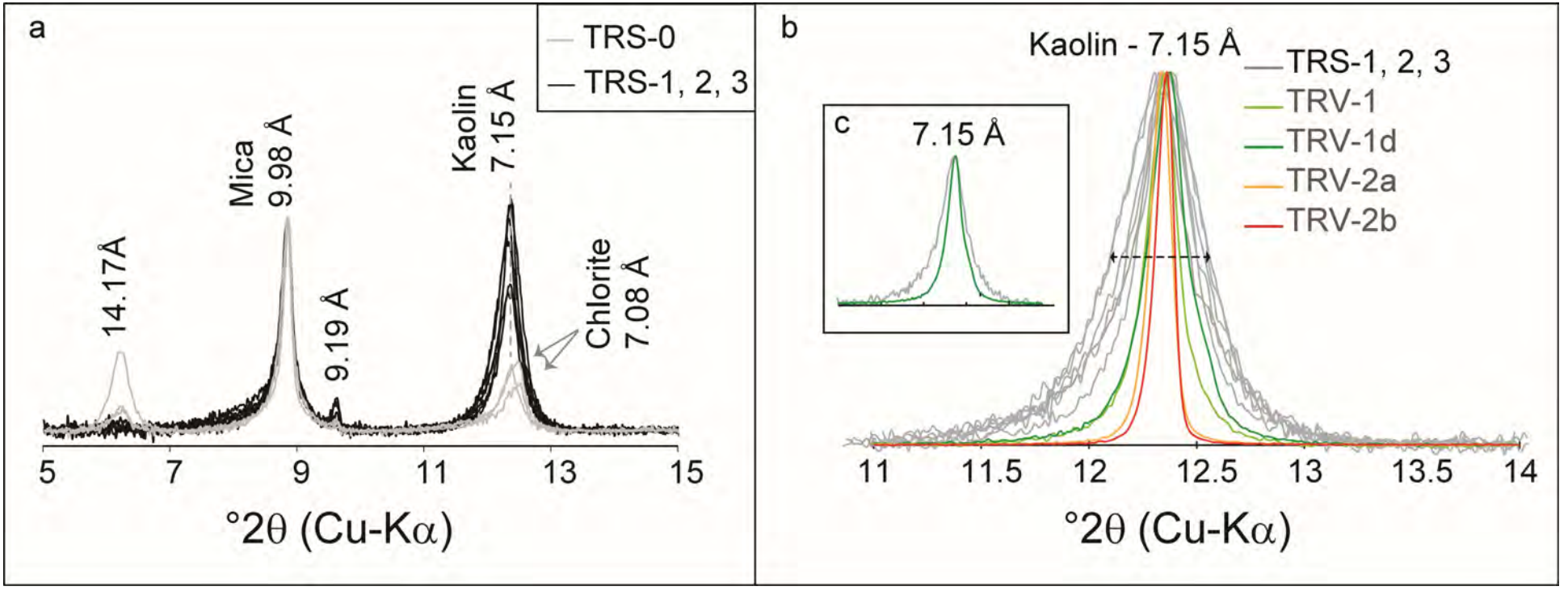
a
TRS-0
TRS-1, 2, 3
14.17Å
Mica
9.98 Å
9.19 Å
Kaolin
7.15 Å
Chlorite
7.08 Å
5
7
9
11
13
15
°2θ (Cu-Kα)
b
Kaolin - 7.15 Å
TRS-1, 2, 3
TRV-1
TRV-1d
TRV-2a
TRV-2b
c
7.15 Å
11
11.5
12
12.5
13
13.5
14
°2θ (Cu-Kα)

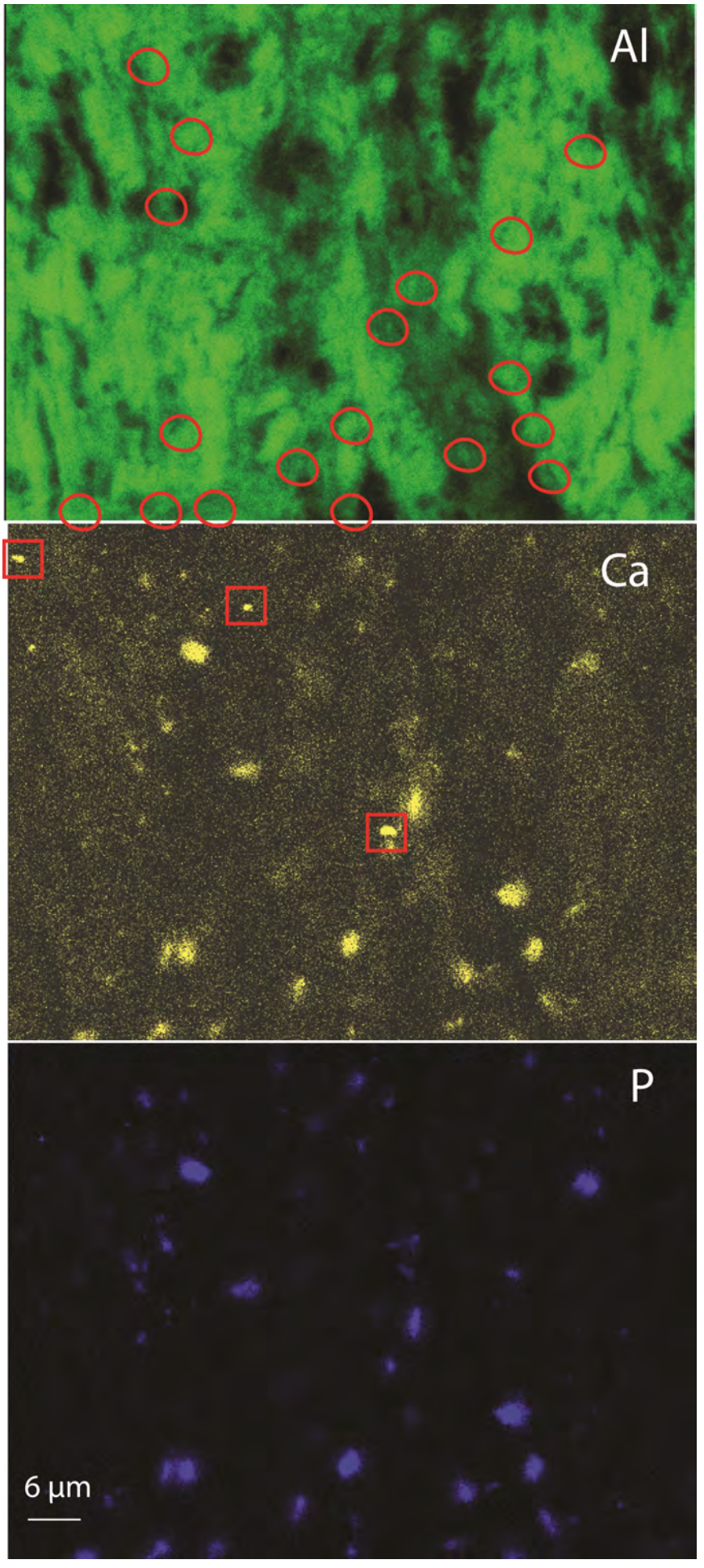
Al
Ca
P
6 µm

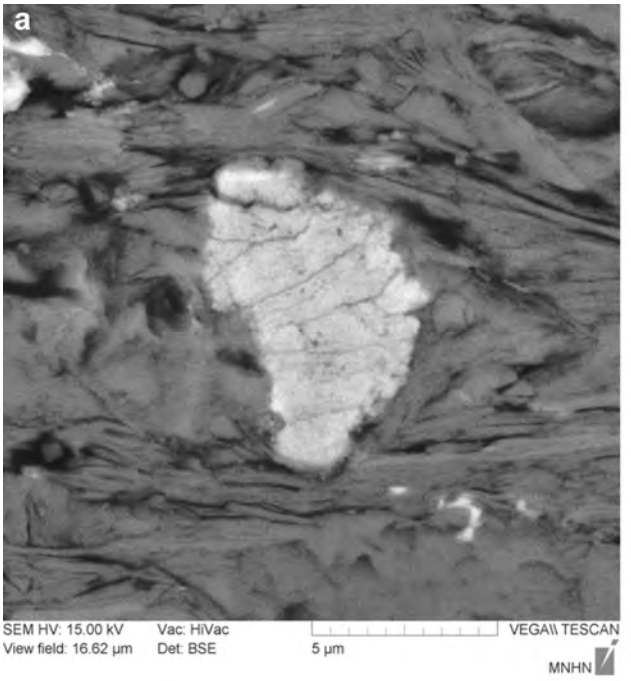
a
SEM HV: 15.00 kV
Vac: HiVac
VEGA\\ TESCAN
View field: 16.62 µm
Det: BSE
5 µm
MNHN

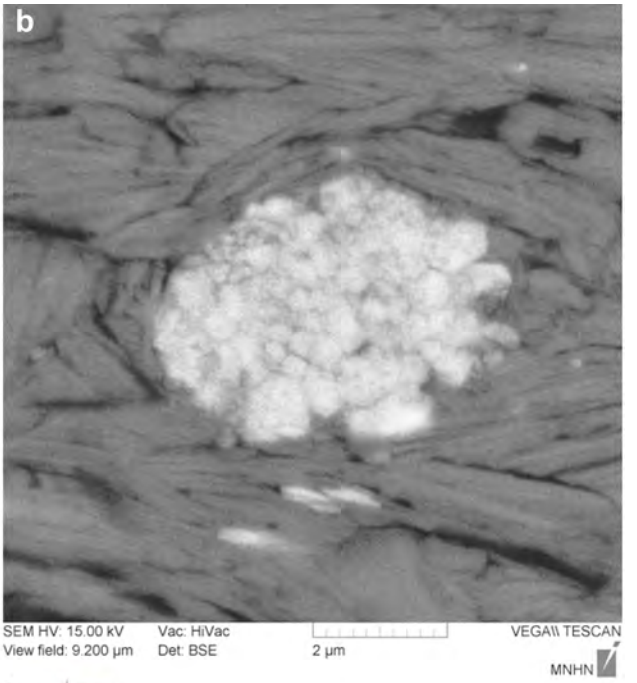
b
SEM HV: 15.00 kV
Vac: HiVac
VEGA\\ TESCAN
View field: 9.200 µm
Det: BSE
2 µm
MNHN

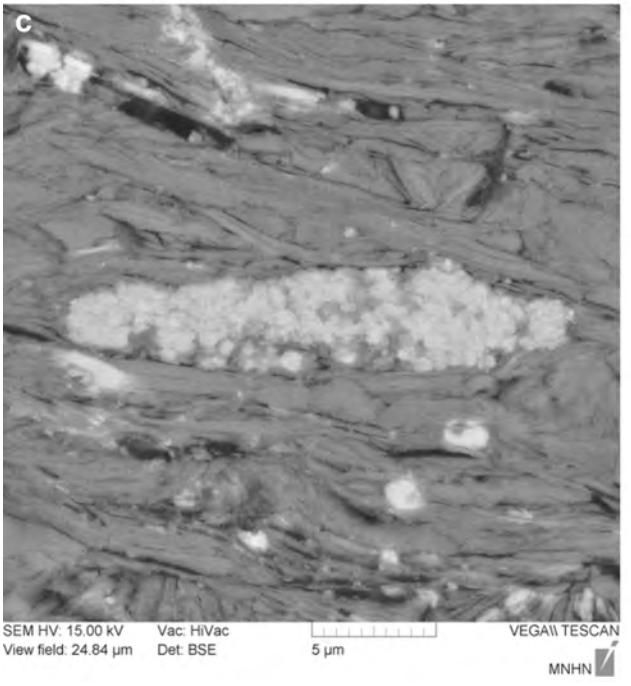
c
SEM HV: 15.00 kV
Vac: HiVac
VEGA\\ TESCAN
View field: 24.84 µm
Det: BSE
5 µm
MNHN

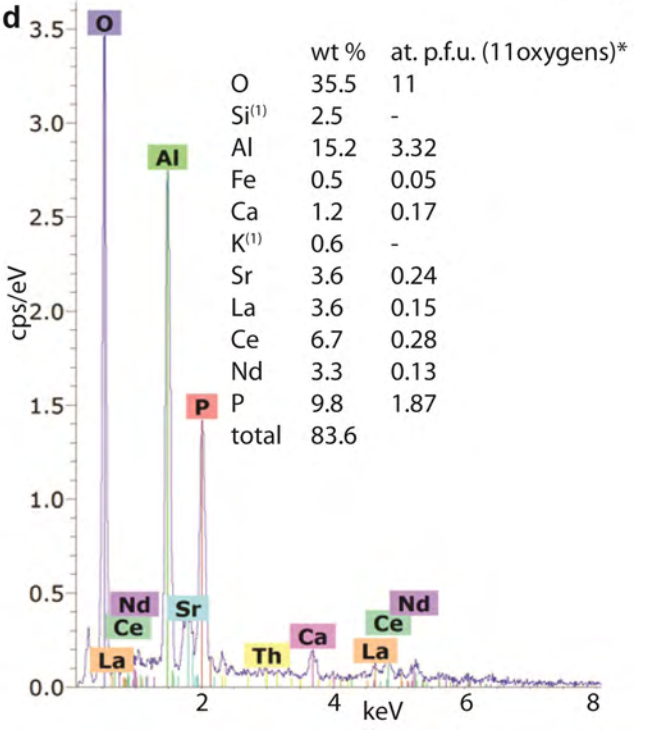
d
cps/eV
keV
O
Al
P
Nd
Ce
La
Sr
Th
Ca
Nd
Ce
La
wt % at. p.f.u. (11oxygens)*
O 35.5 11
Si(1) 2.5 -
Al 15.2 3.32
Fe 0.5 0.05
Ca 1.2 0.17
K(1) 0.6 -
Sr 3.6 0.24
La 3.6 0.15
Ce 6.7 0.28
Nd 3.3 0.13
P 9.8 1.87
total 83.6

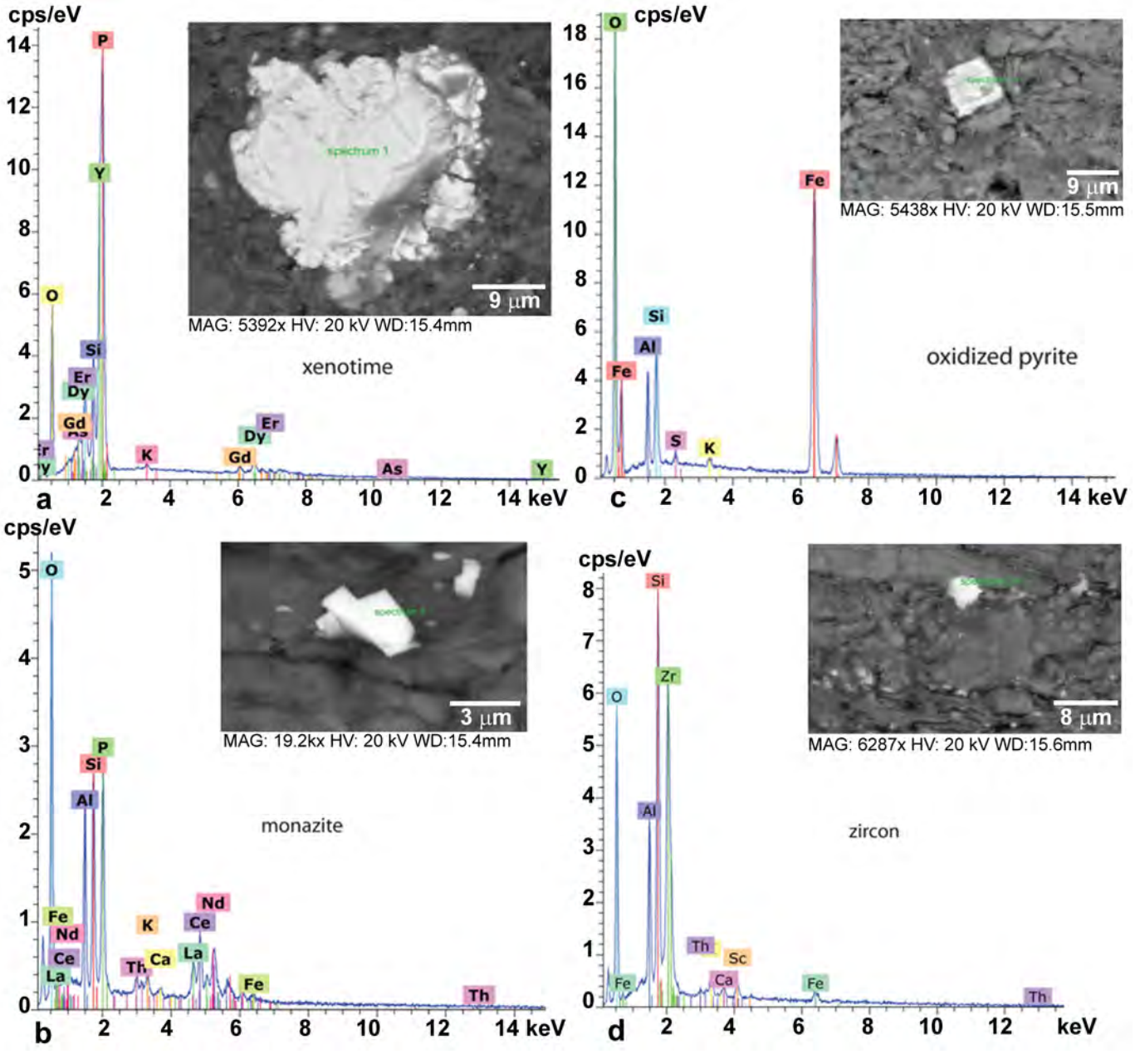

cps/eV
P
Y
O
Si
Er
Dy
Gd
K
Gd
Dy
Er
As
Y
a
2
4
6
8
10
12
14 keV
9 µm
MAG: 5392x HV: 20 kV WD:15.4mm
xenotime
cps/eV
O
Fe
Si
Al
Fe
S
K
c
2
4
6
8
10
12
14 keV
9 µm
MAG: 5438x HV: 20 kV WD:15.5mm
oxidized pyrite
cps/eV
O
P
Si
Al
Fe
Nd
Ce
La
K
Th
Ca
Nd
Ce
La
Fe
Th
b
2
4
6
8
10
12
14 keV
3 µm
MAG: 19.2kx HV: 20 kV WD:15.4mm
monazite
cps/eV
Si
Zr
O
Al
Th
Sc
Ca
Fe
Fe
Th
d
2
4
6
8
10
12
keV
8 µm
MAG: 6287x HV: 20 kV WD:15.6mm
zircon

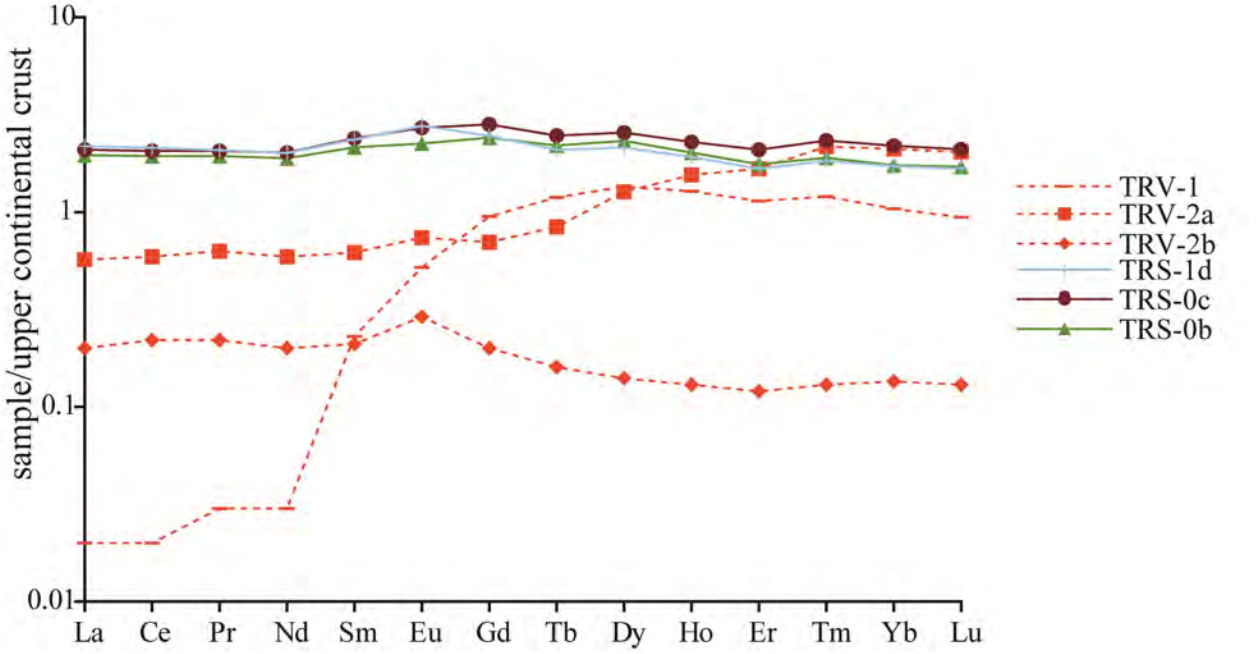
sample/upper continental crust
10
1
0.1
0.01
La
Ce
Pr
Nd
Sm
Eu
Gd
Tb
Dy
Ho
Er
Tm
Yb
Lu
TRV-1
TRV-2a
TRV-2b
TRS-1d
TRS-0c
TRS-0b

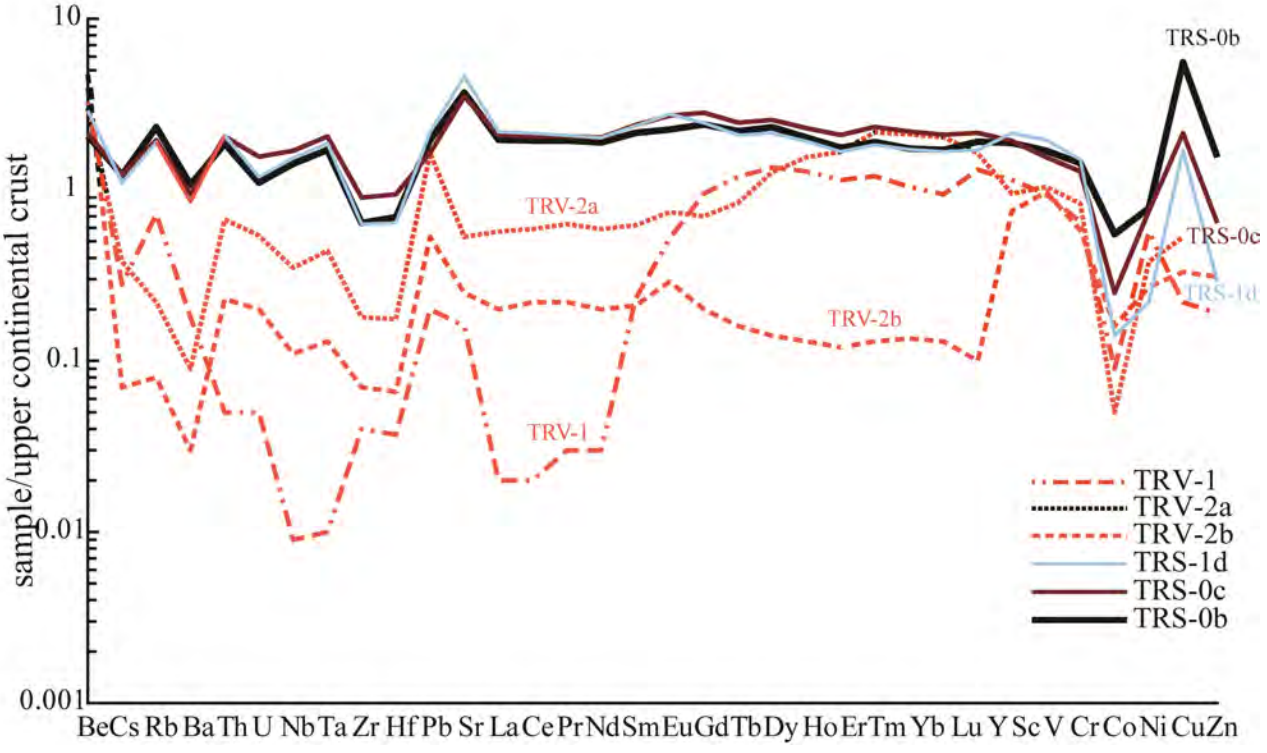
sample/upper continental crust
10
1
0.1
0.01
0.001
Be Cs Rb Ba Th U Nb Ta Zr Hf Pb Sr La Ce Pr Nd Sm Eu Gd Tb Dy Ho Er Tm Yb Lu Y Sc V Cr Co Ni Cu Zn
TRS-0b
TRS-0c
TRS-1d
TRV-2a
TRV-2b
TRV-1
TRV-1
TRV-2a
TRV-2b
TRS-1d
TRS-0c
TRS-0b

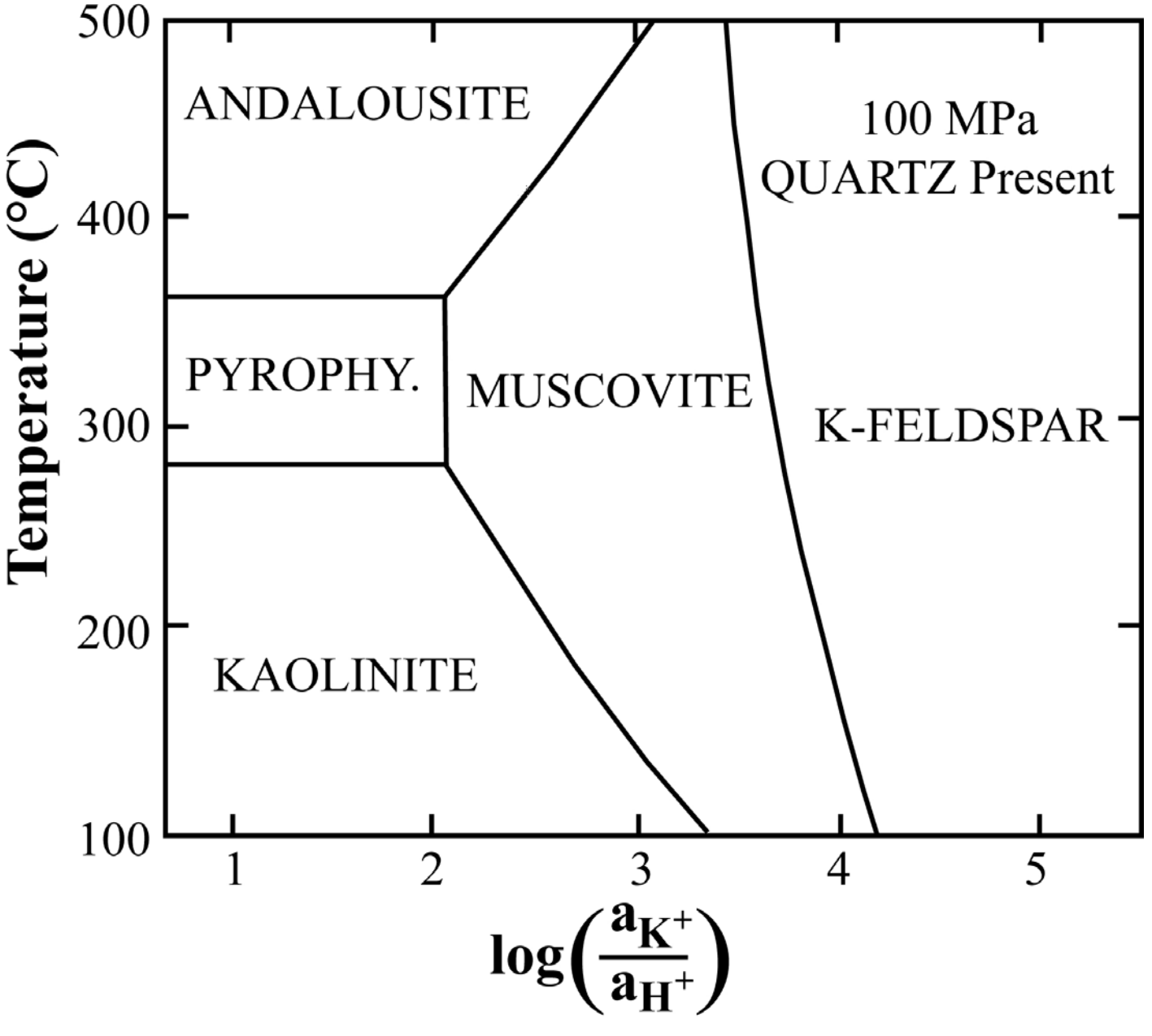
500
400
300
200
100
Temperature (°C)
ANDALOUSITE
100 MPa
QUARTZ Present
PYROPHY.
MUSCOVITE
K-FELDSPAR
KAOLINITE
1
2
3
4
5
$\log\left(\frac{a_{K^+}}{a_{H^+}}\right)$

Table 1. Occurrences of Kaolinite and associated REE phosphates in European Hercynian belt

Massif	Site	Source Rocks	Kaolin deposit references	REE-bearing phosphate minerals	REE references
Massif Central (France)					
Beauvoir, Echassières	1	Granite	Cuney et al., 1992 ; Raimbault et al., 1995	Goyazite, crandallite	Cuney et al., 1992
Cornubian Massif					
St Austell (UK)	2	Granite	Dehain and Filippov, 2015	Monazite	Dehain and Filippov, 2015; Dehain et al.,2019
Rhenish Massif					
Waldsaum (Germany)	3	Keratophyres	Dill et al., 1995	Goyazite, Florencite	Dill et al., 1995 Dill et al., 1995
		Bitumineous shale and volcanics	Dill et al., 1995	Gorceixite	Dill et al., 1995
Bohemian Massif					
Hirschau-Schnaittenbach (Germany)	4	Arkose	Dill, 2017	Unidentified phosphate	Dill, 2017
Pilsen (Czech R.)	5	Arkosic sandstone	Wilson and Jiranek, 1995	Monazite	Höhn et al., 2014
Podborany (Czech R.)	5	Arkosic sandstone	Wilson and Jiranek, 1995	Monazite	Höhn et al., 2014
Karlovy Vary (Czech R.)	5	Granites	Wilson and Jiranek, 1995	Monazite	Höhn et al., 2014
Czerwona Woda, Turow, Dzierzkow (Poland)	6	Limestones	Dill, 2017	Phosphate	Dill, 2017
Strzegom and strzelin (Poland)	7	Granitoids	Kuzvart, 1992	Goyazite	Kuzvart, 1992
Wienzierl-Kriechbau (Austria)	8	Granitoids	Dill, 2017	Monazite	Horn et al., 2014
Mallersbach (Austria)	9	Granitoids	Dill, 2017		
Iberian massif					
Nuevo Montecastelo (Spain)	10	Granitoids	Galán et al., 2007	Monazite, Xenotime	Fernandez-Caliani et al., 2010

Table 2. XRD mineralogy of the TRS and TRV samples (bulk sample analyses). Abbreviations of rock-forming minerals (Whitney and Evans, 2010): Qz: Quartz; Mica: Mica; Sme: Smectite; Chl: Chlorite; Kln: kaolinite; Dck: dickite, N: Nacrite, Prl: Pyrophyllite; Flo: Florencite; Rt: Rutile; Gth: Goethite; Hem: Hematite; Jrs: Jarosite. *Identified from glycolated oriented clay fractions, + major mineral, (+) minor mineral.

	Color	Sample	Qz	Mica	Sme*	Chl	Kln	Dck	N	Prl	Flo	Rt	Gth	Hem	Jrs
Schist															
friable	*bleached*	TRS-3	+	+			+				(+)	+			
		TRS-2	+	+			+					+			
		TRS-1d	+	+		(+)	+			(+)	(+)	+			
friable	*dark*	TRS-1c	+	+			+				(+)	+			
	grey	TRS-1b	+	+			+			(+)		+			
		TRS-1a	+	+			+			(+)		+			
		TRS-0c	+	+		+	+			(+)	(+)	+			
indurated	*grey*	TRS-0b	+	+		+	+			(+)	(+)	+			
		TRS-0a	+	+		+	+			(+)		+			
Fissure															
	white	TRV-1	+	+	(+)	(+)	+	+	+	+					
	white	TRV-1d	+	(+)		+	+	+	+	+	?				
	yellow	TRV-2a	(+)					+	+						
	orange	TRV-2b	(+)					+	+				(+)	(+)	
	yellow	TRV-3													+

Table 3. Major element contents of Tertre Rouge samples (wt%).

Element	TRS-0b	TRS-0c	TRS-1d	TRV-1	TRV-2a	TRV-2b
SiO_2	54.99	58.72	53.23	55.19	45.9	46.36
TiO_2	1.06	1.21	1.14	0.01	0.26	0.08
Al_2O_3	26.52	25.28	29.5	34.05	37.45	38.14
Fe_2O_3	4.48	1.98	2.99	0.21	2.94	2.77
MgO	0.79	0.52	0.27	0.13	0.05	0.02
MnO	0.006	n.d.	n.d.	n.d.	n.d.	n.d.
CaO	0.13	0.13	0.16	0.07	0.06	0.11
Na_2O	0.82	0.92	0.85	0.21	0.09	0.02
K_2O	3.93	3.32	3.24	1.07	0.34	0.1
P_2O_5	0.25	0.25	0.4	0.03	0.13	0.07
L.O.I.	7.46	7.86	8.97	9.62	13.77	13.51
Total	*100.44*	*100.18*	*100.75*	*100.58*	*100.98*	*101.18*
Organic C	0.23	0.89	0.58	n.a.	n.a.	n.a.

L.O.I. : loss on ignition; n.d. : not detected; n.a.: not analyzed

Table 4. Trace element contents of Tertre Rouge samples (ppm).

Element	TRS-0b	TRS-0c	TRS-1d	TRV-1	TRV-2a	TRV-2b
Be	4.35	4.5	6.07	6.85	6.27	9.81
V	164	150	190	91	100	94.5
Cr	132	118	142	59.2	76.8	52.9
Co	9.56	4.41	2.46	1.68	0.78	2.8
Ni	36.7	35.4	10.5	26.7	17.8	12.6
Cu	156	59.8	47.4	6.2	14.8	9.2
Zn	104	43.1	19.3	12.7	n.d.	20.5
Cd	0.03	0.17	0.14	n.d.	n.d.	n.d.
Ga	35.1	33	40	26.4	22.5	19.1
Ge	3.36	3.70	3.76	2.59	1.84	1.73
As	12.2	5.93	42.4	1.07	39.3	16.7
In	0.1	0.12	0.14	0.06	0.13	0.11
Sc	26.41	27.06	29.98	15.99	13.28	10.45
Mo	n.d.	0.54	0.56	0.81	0.52	n.d.
Sn	15.8	8.54	6.92	2.00	2.79	1.35
Sb	0.32	0.25	0.41	1.48	0.25	0.35
Cs	5.99	5.98	5.39	1.37	1.87	0.35
Ba	670	587	531	111	58.9	18.4
W	2.4	2.29	2.43	1.39	n.d.	n.d.
Pb	33.3	27.6	36.9	3.47	14	9.09
Bi	0.4	0.46	0.35	n.d.	0.13	0.14
As	12.2	5.93	42.4	1.07	39.3	16.7
Sr	1179	1117	1417	50.4	169	79.7
Rb	195	165	161	60.6	18.2	4.74
Th	19.5	21.2	21.8	0.43	7.06	2.4
U	2.97	4.24	3.2	0.13	1.47	0.55
La	60.8	64.8	67.7	0.622	17.8	6.2
Ce	122	130	135	1.48	37.3	13.6
Pr	13.8	14.6	14.8	0.201	4.43	1.59
Nd	51	54.6	54.5	0.917	16.1	5.59
Sm	10.1	11.2	11.1	1.07	2.91	1.01
Eu	2.25	2.71	2.77	0.513	0.742	0.285
Gd	9.64	11.3	9.85	3.81	2.78	0.8
Tb	1.54	1.73	1.46	0.828	0.587	0.104
Dy	9.04	10	8.34	5.28	4.98	0.565
Ho	1.68	1.9	1.58	1.06	1.29	0.104
Er	4.06	4.8	3.83	2.61	3.85	0.269
Tm	0.57	0.698	0.549	0.36	0.647	0.04
Yb	3.47	4.38	3.44	2.08	4.22	0.269
Lu	0.527	0.653	0.515	0.291	0.632	0.041
Y	39.6	45.2	36	27.5	34.3	2.1
Zr	125	174	120	8.05	33.9	13.2
Hf	3.64	4.97	3.36	0.37	0.93	0.35
Nb	17	20.3	18.4	0.11	4.18	1.3
Ta	1.54	1.85	1.68	0.01	0.39	0.12

L.O.I. : loss on ignition; n.d. : not detected; n.a.: not analyzed

Table S1. Correlation coefficient matrix for trace elements (correlation coefficients $r^2 > 0.9$ in bold) (P for phosphates; TiO_2 for rutile; K_2O for muscovite/illite).

	As	Ba	Be	Bi	Co	Cr	Cs	Cu	Ga	Ge	Hf	In	Mo	Nb	Pb	Rb	Sb	Sc	Sn	Sr	Ta	Th	U	V	W	Y	Zn	Zr	La	Lu
As		0	0	0.2	0.12	0	0	0	0	0	0	0.67	0.43	0	0.11	0	0.23	0	0	0	0	0	0	0.1	0.34	0	0	0	0	0
Ba			0.65	**0.93**	0.54	0.88	**0.97**	0.70	0.82	0.86	0.89	0.0	0.2	0.9	**0.98**	0.83	0.12	0.91	0.82	**0.90**	**0.90**	0.88	0.80	0.82	**0.92**	0.5	0.46	0.87	**0.90**	0.34
Be				0.6	0.28	0.58	0.73	0.48	0.52	0.56	0.62	0	0.35	0.58	0.44	0.66	0	0.59	0.6	0.5	0.57	0.56	0.58	0.4	0.51	**0.95**	0.4	0.6	0.55	0.77
Bi					0.39	0.73	**0.91**	0.46	0.70	0.90	**0.98**	0	0.6	**0.94**	0.71	**0.91**	**0**	0.84	0.62	0.81		0.87	0.90	0.66	**0.96**	0.52	0.32	**0.97**	0.88	0.26
Co						0.3	0.40	**0.92**	0.21	0.23	0.34	0	0	0.32	0.32	0.51	0	0.26	**0.90**	0.31	0.31	0.29	0.29	0.26		0.10	**0.99**	0.31	0.31	0
Cr							**0.92**	0.53	0.89	0.80	0.78	0.22	0.38	0.90	**0.96**	0.86	0.2	**0.92**	0.66	**0.97**	0.91	**0.95**	**0.80**	**0.96**		0.54	0.27	0.79	**0.96**	0.44
Cs								0.59	0.82	0.85	**0.93**	0.1	0.31	**0.95**	0.85	**0.94**	0.16	**0.92**	0.74	**0.91**	**0.95**	**0.94**	0.89	0.84	**0.95**	0.66	0.36	**0.92**	**0.95**	0.50
Cu									0.32	0.35	0.46			0.46	0.52	0.65	0.13	0.47	**0.97**	0.48	0.47	0.47	0.37	0.43	0.43	0.27	**0.95**	0.43	0.49	0.16
Ga										0.91	0.92	0	0	0.76	0.78	0.88	0	**0.97**	0.51	0.88	0.76	0.77	0.80	0.89	0.81	0.52	0.13	0.65	0.79	0.30
Ge											0.79	0	0	0.81	0.18	0.91	0	**0.96**	0.50	0.84	0.81	0.76	0.69	0.78	0.88	0.54	0.12	0.78	0.79	0.30
Hf												0.13		**0.96**	0.75	0.82	0.23	0.82	0.61	0.84	**0.96**	**0.91**	**0.96**	0.70	0.77	0.57	0.27	**1**	0.91	0.46
In													nd	0.22	0.33	0.0	0	0.1	0	0.21	0.22	0.24	0.28	0.25	0.79	0	0	0.16	0.26	0.19
Mo														0.48	0.48		**0.99**	0.1	0.3	0.28	0.40	0.48	0.50	0.26		0.53	0.49	0.35	0.43	0.49
Nb															0.89	0.86	0.27	0.89	0.62	**0.95**	**1**	**0.99**	**0.96**	0.86	**0.94**	0.53	0.75	**0.97**	**0.99**	0.44
Pb																0.76	0.33	0.83	0.62	**0.95**	0.9	**0.95**	0.80	**0.96**	**0.98**	0.4	0.88	0.77	**0.95**	0.36
Rb																	0	**0.93**	0.78	0.87	0.84	0.81	0.72	0.80	**0.93**	0.55	0.42	0.8	0.84	0.31
Sb																			0.15		0.27	0.31	0.36			0	0.19	0.26	0.26	0.14
Sc																			0.57	**0.94**	0.89	0.88	0.76	**0.90**	**0.96**	0.57	0.17	0.81	**0.9**	0.37
Sn																				0.62	0.61	0.61	0.52	0.55	0.55	0.40	0.86	0.57	0.63	0.36
Sr																					**0.95**	**0.96**	0.83	**0.98**	**0.98**	0.44	0.23	0.84	**0.97**	0.33
Ta																						**0.99**	**0.96**	0.86	**0.94**	0.53	0.25	**0.97**	**0.99**	0.44
Th																							**0.94**	0.90	**0.97**	0.53	0.20	0.46	**1**	0.47
U																								0.73	0.83	0.56	0.21	**0.97**	**0.93**	0.54
V																										0.37	0.17	0.72	**0.92**	0.28
P	0.22	0.46		0.52	0.11	**0.90**	0.72	0.27	0.79	0.66	0.64	0.44	0.4	0.81	**0.93**	0.62	0.26	0.80	0.38	**0.90**	0.81	0.87	0.72	**0.95**	0.84	0.35	0	0.66	0.87	0.34
TiO_2		0.92	0.57	0.92	0.33	0.93	0.96	0.48	0.78	0.82	0.95	0.22	0.34	1	0.92	0.85	0.27	0.90	0.63	0.96	1	0.99	0.95	0.88	0.96	0.52	0.27	**0.96**	**1**	0.43
K_2O		**0.99**	0.65	0.90	0.52	0.87	**0.95**	0.66	0.86	**0.90**	0.84	0	0	0.86	0.79	**1**	0.88	**0.93**	0.79	0.88	0.86	0.83	0.73	0.81	**0.94**	0.54	0.44	0.82	0.85	0.32

Declaration of interests

+ The authors declare that they have no known competing financial interests or personal relationships that could have appeared to influence the work reported in this paper.

☐The authors declare the following financial interests/personal relationships which may be considered as potential competing interests: